arXiv:1610.01055v2 [astro-ph.EP] 11 Oct 2016

Homing in for New Year: impact parameters and pre-impact orbital evolution of meteoroid 2014 AA

C. de la Fuente Marcos • R. de la Fuente Marcos • P. Mialle

Abstract On 2008 October 7, small asteroid 2008 TC_3 turned itself into the parent body of the first meteor ever to be predicted before entering the Earth's atmosphere. Over five years later, the 2014 AA event became the second instance of such an occurrence. The uncertainties associated with the pre-impact orbit of 2008 TC_3 are relatively small because thousands of observations were made during the hours preceding the actual meteor airburst. In sharp contrast, 2014 AA was only observed seven times before impact and consequently its trajectory is somewhat uncertain. Here, we present a recalculation of the impact parameters — location and timing— of this meteor based on infrasound recordings. The new values —($\lambda_{\rm impact}$, $\phi_{\rm impact}$, $t_{\rm impact}$) = (-44°, +11°, 2456659.618 JD UTC)— and their uncertainties together with Monte Carlo and N-body techniques, are applied to obtain an independent determination of the pre-impact orbit of 2014 AA: $a = 1.1623$ AU, $e = 0.2116$, $i = 1\overset{\circ}{.}4156$, $\Omega = 101\overset{\circ}{.}6086$, and $\omega = 52\overset{\circ}{.}3393$. Our orbital solution is used to investigate the possible presence of known near-Earth objects (NEOs) moving in similar orbits. Among the objects singled out by this search, the largest is 2013 HO_{11} with an absolute magnitude of 23.0 (diameter 75–169 m) and a MOID of 0.006 AU. Prior to impact, 2014 AA was subjected to a web of overlapping secular resonances and it followed a path similar to those of 2011 GJ_3, 2011 JV_{10}, 2012 DJ_{54}, and 2013 NJ_4. NEOs in this transient group have their orbits controlled by close encounters with the Earth–Moon system at perihelion and Mars at aphelion, perhaps constituting a dynamical family. Extensive comparison with other studies is also presented.

Keywords Celestial mechanics · Minor planets, asteroids: individual: 2014 AA · Minor planets, asteroids: individual: 2011 GJ_3 · Minor planets, asteroids: individual: 2011 JV_{10} · Minor planets, asteroids: individual: 2012 DJ_{54} · Minor planets, asteroids: individual: 2013 NJ_4 · Planets and satellites: individual: Earth

1 Introduction

On 2014 January 2, asteroid 2014 AA became the second example of an object discovered just prior to hitting the Earth (Brown 2014; Jenniskens 2014). Over five years before this event occurred, similarly small 2008 TC_3 had stricken our planet hours after being first spotted (Chodas et al. 2009; Jenniskens et al. 2009; Oszkiewicz et al. 2012). The fireball caused by the entry of 2008 TC_3 was observed by the Meteosat 8 weather satellite (Borovička & Charvát 2009); no images of the atmospheric entry of 2014 AA have emerged yet, although there is robust evidence for an impact over the Atlantic Ocean (Chesley et al. 2015; Farnocchia et al. 2016) less than a day after this small asteroid was discovered.

The uncertainty associated with the pre-impact orbit of 2008 TC_3 is relatively small because thousands of observations were made during the hours preceding the actual strike (Chodas et al. 2009; Jenniskens et al. 2009; Kozubal et al. 2011; Oszkiewicz et al. 2012). In sharp contrast, 2014 AA was only observed seven times before impact (Kowalski et al. 2014) and consequently its pre-impact orbit is somewhat uncertain (Chesley et al. 2014, 2015; Farnocchia et al. 2016). Both objects hit the Earth about 20 hours after they were first detected (Farnocchia et al. 2015). Asteroid 2008 TC_3

C. de la Fuente Marcos

R. de la Fuente Marcos

Apartado de Correos 3413, E-28080 Madrid, Spain

P. Mialle

Provisional Technical Secretariat, Comprehensive Nuclear-Test-Ban Treaty Organisation, PO Box 1200, Vienna 1400, Austria

completely broke up over northern Sudan on 2008 October 7 (Jenniskens et al. 2009); asteroid 2014 AA probably met a similar end over the Atlantic Ocean. Meteorites were collected from 2008 TC_3 (Jenniskens et al. 2009); any surviving meteorites from 2014 AA were likely lost to the sea.

Both 2008 TC_3 and 2014 AA had similar sizes of a few metres. Such small asteroids or meteoroids (diameter < 10 m) are probably fragments of larger objects, which may also be fragments themselves. The study of the orbital dynamics of such fragments is a subject of considerable practical interest because small bodies dominate the risk of unanticipated Earth impacts with just local effects (Brown et al. 2013). Asteroid fragmentation could be induced by collisional processes (e.g. Dorschner 1974; Ryan 2000) but also be the combined result of thermal fatigue (e.g. Čapek & Vokrouhlický 2010) and rotational (e.g. Walsh et al. 2008) or tidal stresses (e.g. Richardson et al. 1998; Tóth et al. 2011). The present-day rate of catastrophic disruption events of asteroids in the main belt has been recently studied by Denneau et al. (2015). These authors have found that the frequency of this phenomenon is much higher than previously thought, with rotational disruptions being the dominant source of fragments. Production of fragments can be understood within the context of active asteroids (see e.g. Jewitt 2012; Jewitt et al. 2015; Drahus et al. 2015; Agarwal et al. 2016).

Here, we revisit the topic of the impact parameters of 2014 AA, then apply Monte Carlo and N-body techniques to obtain an independent determination of the pre-impact orbit of 2014 AA. The computed orbital solution is used to investigate the existence of near-Earth objects (NEOs) moving in similar orbits. This paper is organized as follows. In Sect. 2, we review what is currently known about 2014 AA. The atmospheric entry of 2014 AA is revisited in Sect. 3; an improved impact solution (location and timing), that is based on a refined analysis of infrasound recordings, is presented. A Monte Carlo technique is used in Sect. 4 to estimate the most probable, in geometric terms, pre-impact orbit. An N-body approach is described and applied in Sect. 5 to obtain a more realistic orbital solution. In Sect. 6, we provide an extensive and detailed comparison with results obtained by other authors and show that all the solutions published so far are reasonably consistent. Based on the new solution, the recent past orbital evolution of 2014 AA is reconstructed in Sect. 7. A number of perhaps dynamically-related small bodies are discussed in Sect. 8. Section 9 summarizes our conclusions.

2 Asteroid 2014 AA

Asteroid 2014 AA was discovered on 2014 January 1 by R. A. Kowalski using the 1.5-m telescope of the Mount Lemmon Survey in Arizona (Kowalski et al. 2014), becoming the first asteroid identified in 2014. It was initially observed at a V-magnitude of 19.1 and found to be a very small body with $H = 30.9$ mag which translates into a diameter in the range 1–4 m for an assumed albedo of 0.20–0.04. The available orbits of this Apollo meteoroid are based on just seven astrometric observations for a data-arc span of 1 hour and 9.5 minutes; therefore, its actual path is poorly constrained (see Table 1 for the orbits computed by the Solar System Dynamics Group or SSDG).[1,2] With a value of the semi-major axis of 1.16 AU, its eccentricity was moderate, $e = 0.21$, and its inclination very low, $i = 1\overset{\circ}{.}4$. Its Minimum Orbit Intersection Distance (MOID) with our planet was 4.5×10^{-7} AU and it orbited the Sun with a period of 1.25 yr. This type of orbit is only directly perturbed by the Earth–Moon system (at perihelion) and Mars (at aphelion).

In spite of the uncertain orbit, independent calculations carried out by Bill Gray, the Minor Planet Center (MPC), and Steven R. Chesley at the Jet Propulsion Laboratory (JPL) all claimed a virtually certain collision between 2014 AA and our planet to occur on 2014 January 2.2±0.4 (Kowalski et al. 2014); in particular, Steven R. Chesley predicted impact locations along an arc extending from Central America to East Africa.[3] Using data from the Comprehensive Nuclear-Test-Ban Treaty Organization (CTBTO) infrasound sensors, Steven R. Chesley, Peter Brown, and Peter Jenniskens computed a probable impact location; Steven R. Chesley pointed out that the impact time could have been 2014 January 2 at 4:02 UTC, with a temporal uncertainty of tens of minutes, and the impact location coordinates could have been $11\overset{\circ}{.}7$ N, $318\overset{\circ}{.}7$ E (or $41\overset{\circ}{.}3$ W) with a spatial error of a few hundred kilometres.[4]

Chesley et al. (2015) have released the hypocentre location solution for the 2014 AA impact (see their table 1) as included in the Reviewed Event Bulletin (REB) of the International Data Centre (IDC) of the CTBTO for 2014 January 2. This impact solution has

[1]The orbit available from the Minor Planet Center is: $a = 1.1605495$ AU, $e = 0.2092087$, $i = 1\overset{\circ}{.}39894$, $\Omega = 101\overset{\circ}{.}70409$, and $\omega = 52\overset{\circ}{.}02425$, referred to the epoch 2456600.5 JD TDB.

[2]The orbit available from NEODyS-2 is: $a = 1.17\pm0.03$ AU, $e = 0.22\pm0.03$, $i = 1\overset{\circ}{.}4\pm0\overset{\circ}{.}2$, $\Omega = 101\overset{\circ}{.}57\pm0\overset{\circ}{.}12$, and $\omega = 52^\circ\pm1^\circ$, referred to the epoch 2456658.3 JD TDB.

[3]http://neo.jpl.nasa.gov/news/news182.html

[4]http://neo.jpl.nasa.gov/news/news182a.html

Table 1 Heliocentric Keplerian orbital elements of 2014 AA from the JPL Small-Body Database and HORIZONS On-Line Ephemeris System. Values include the 1σ uncertainty. The orbits are computed at epoch JD 2456658.5 that corresponds to 0:00 TDB on 2014 January 1. The orbit in the left-hand column was computed on 2014 June 13 18:59:39 UT and it is based on seven astrometric observations; the orbit in the column next to it was computed on 2015 April 13 00:35:03 UT and it is based on eight observations (seven astrometric and one infrasounds-based). The third orbit is the one currently available; it was computed on 2016 January 13 11:17:04 UT and, as the previous one, is based on seven astrometric observations and one infrasounds-based (Farnocchia et al. 2016). Values in parentheses are referred to epoch JD 2456658.628472222 that corresponds to 03:05:00.0000 TDB on 2014 January 1 (or nearly 24 h before impact time) and are based on the orbital solution displayed in the column next to it (J2000.0 ecliptic and equinox).

Semi-major axis, a (AU)	=	1.16±0.03	1.163±0.011	1.162±0.004	(1.162312786616874)
Eccentricity, e	=	0.21±0.03	0.213±0.011	0.211±0.004	(0.2116141752291786)
Inclination, i (°)	=	1.4±0.2	1.42±0.07	1.41±0.03	(1.415646256117421)
Longitude of the ascending node, Ω (°)	=	101.58±0.12	101.61±0.02	101.613±0.010	(101.6086439360293)
Argument of perihelion, ω (°)	=	52.3±1.2	52.4±0.5	52.3±0.2	(52.33920188906649)
Mean anomaly, M (°)	=	324.2±1.3	324.1±0.4	324.0±0.2	(324.1460200866331)
Time of perihelion passage, τ (JD TDB)	=	2456245±16	2456704.24±0.06	2456704.22±0.02	(2456704.213037788402)
Perihelion, q (AU)	=	0.916±0.009	0.916±0.004	0.917±0.002	(0.9163509249186160)
Aphelion, Q (AU)	=	1.41±0.03	1.411±0.013	1.407±0.005	(1.408274648315132)
Absolute magnitude, H (mag)	=	30.9			

been utilized in Farnocchia et al. (2016) to further improve the trajectory of 2014 AA. The impact time was 2014 January 2 at 3:05:25 UTC with an uncertainty of 632 s (epoch JD 2456659.628762±0.007315). The impact location coordinates were latitude (°N) equal to $+14\overset{\circ}{.}6326$ and longitude (°E) of $-43\overset{\circ}{.}4194$ with an uncertainty of about $3\overset{\circ}{.}5\times1\overset{\circ}{.}4$ and a major axis azimuth of 76°(clockwise from N, see fig. 5 in Chesley et al. 2015). These values and those from the improved impact solution presented in the following section are used here as constraints to compute the pre-impact orbit of 2014 AA. Our approaches do not initially rely on actual astrometric observations of this meteoroid obtained prior to its impact, but on Keplerian orbits (geometry) and Newtonian gravitation (N-body calculations). None the less, the available astrometry is used later to further refine our orbital solution. Therefore, our favoured orbital solution combines the original, ground-based optical astrometry and infrasound data.

3 An improved determination of the hypocentre location

The IDC of the CTBTO in Vienna processes automatically and in near real time continuous recordings from the globally deployed International Monitoring System (IMS) infrasound stations. The IDC automatic system is designed to detect close-to-the-ground, explosion-like signals. Station detections are associated to form events. The system can automatically associate signal detections at distances up to 6,700 km (or 60°) from the source location; for larger propagation distances the signals are manually associated with the event. The signal from the impact of 2014 AA was automatically detected by the IDC automatic system. The reviewed analysis carried out in the hours following the event (published in the REB) provided a refined list of infrasound signals associated with the meteor as well as an improved source location based on infrasound recordings.

In the REB of the IDC, signals recorded at three IMS infrasound stations were associated to build an event in the Atlantic, 1,450 km to the north-east of French Guyana, at coordinates ($14\overset{\circ}{.}63$ N, $43\overset{\circ}{.}42$ W) with an error ellipse of 390.4 km×154.8 km (semi-major axis×semi-minor axis) and a major axis azimuth of $76\overset{\circ}{.}4$. The source origin time of the main blast was estimated at 03:05:25 UTC with an origin time error of about 630 s. The three IMS infrasound stations that recorded the airburst are located at large distances, ranging from 2,900 to 4,400 km from the REB location, one located to the north-west in the Northern Hemisphere and two to the south-west across the Equator (see Fig. 1). For further technical details, see sect. 2.2 in Farnocchia et al. (2016).

The IDC system makes use of back-azimuths (or direction of arrivals) and times from the associated detections to localize and estimate the origin time of infrasound events. In order to associate signals and localize acoustic events, travel-time tables are used and these are based on an empirical celerity model (Brachet et al. 2010) that allows for fast computations as required by the IDC operational system. Celerity, or propagation speed of the wave, is the horizontal propagation distance between its origin and the detecting station divided by its associated travel-time in the atmosphere. The back-azimuths and travel-times for each individual station are not corrected to account for atmospheric effects during the propagation of the waves.

The combination of both parameters (back-azimuths and times) for the localization explains the separation between the actual location in the REB and the area of cross bearing of the three detections. The acoustic source altitude and its extension are not considered for the REB solution in space as the CTBTO infrasound system has been built to monitor a close-to-the-ground, explosion-like source, i.e. a point source rather than a line source. However, given the distance from the airburst to the detecting stations and the specificity of the acoustic source generated by the airburst of 2014 AA, a realistic approximation for the location and origin time estimations is to consider only the three directions of arrival and the detection time of the closest station to the north-west as the travel-time model does not account for paths crossing the Equator. This corrected solution leads to an event location at the intersection of the back-azimuth (11.°22 N, 43.°71 W) and an origin time of 2014 January 2 02:49:36 UTC (epoch JD 2456659.617778±0.011087) with an error ellipse of dimensions 678 km×404 km, major axis azimuth 180°, and origin time error in excess of 1500 s. The new solution for the hypocentre location of the 2014 AA impact is given in Table 2 and its location shown in Fig. 1.

The value of the time uncertainty illustrates the large variability of the infrasound event origin in time due to the heterogeneity of the atmosphere in space and time, the source altitude, and the source displacement, which are currently not fully captured by the IDC system. In principle, the location of the airburst could be refined using atmospheric propagation modelling with real-time accurate atmospheric datasets. However, it would also be difficult to constrain the solution better given the limited number of observations (three) and the numerous hypotheses made on the propagation ranges, the uncertainty of the meteorological models in the stratosphere, and the source altitude and dimensions in space and time.

Table 2 Hypocentre location solution for the 2014 AA impact on 2014 January 2. Impact coordinates include the 1σ uncertainty.

Time (UTC)	=	02:49:36.45
Time uncertainty (s)	=	957.898
Latitude (°N)	=	+11.2±2.8
Longitude (°E)	=	−43.7±1.7
Confidence region at 0.90 level:		
Semi-major axis (km, °)	=	677.6, 6.09
Semi-minor axis (km, °)	=	404.4, 3.64
Major axis azimuth (°)	=	179.7 (clockwise from N)
Time uncertainty (s)	=	1576.9

4 Pre-impact orbit: geometric approach

Following the approach implemented in de la Fuente Marcos & de la Fuente Marcos (2013, 2014), we have used the published impact time and coordinates —see sect. 3 in Chesley et al. (2015) and our own Sect. 3 above— to investigate the pre-impact orbit of 2014 AA. The methodology applied in this section is simple and entirely geometric.

4.1 A purely geometric Monte Carlo approach

Let us consider a planet and an incoming natural object, the parent body of a future meteor. Eventually a collision takes place, and the impact time and coordinates of the impact site on the atmosphere of the planet are reasonably well determined. The objective is computing the path of the impactor prior to hitting the planet. Let us assume that, instantaneously, both the orbit of the planet and that of the putative impactor are Keplerian ellipses (their osculating trajectories). Under the two-body approximation, the equations of the orbit around the Sun of any body (planetary or minor) in space are given by the expressions (see e.g. Murray & Dermott 1999):

$$\begin{aligned} X &= r\ (\cos\Omega\cos(\omega+f) - \sin\Omega\sin(\omega+f)\cos i) \\ Y &= r\ (\sin\Omega\cos(\omega+f) + \cos\Omega\sin(\omega+f)\cos i) \\ Z &= r\ \sin(\omega+f)\sin i \end{aligned} \quad (1)$$

where $r = a(1-e^2)/(1+e\cos f)$, a is the semi-major axis, e is the eccentricity, i is the inclination, Ω is the longitude of the ascending node, ω is the argument of perihelion, and f is the true anomaly. At the time of impact, the osculating elements of the planet (a_p, e_p, i_p, Ω_p, ω_p, and f_p) are well established. In a general case, the impact time, t_impact, is known within an uncertainty interval Δt_impact. This implies that the osculating elements of the planet may also be affected by their respective uncertainties (Δa_p, Δe_p, Δi_p, $\Delta\Omega_\mathrm{p}$, $\Delta\omega_\mathrm{p}$, and Δf_p). Let us assume that immediately before striking, the impactor was moving around the Sun in an orbit with certain values of the osculating elements (a, e, i, Ω, and ω); in this case, the minimum distance between the planet and the orbit of the virtual impactor at the time of impact can be easily estimated using Monte Carlo techniques (Metropolis & Ulam 1949; Press et al. 2007).

Given a set of osculating elements for a certain object, the above equations are randomly sampled in true anomaly for the object and the position of the planet at the time of impact is used to compute the usual Euclidean distance between both points (one on the orbit

and the other one being the location of the planet) so the minimum distance is eventually found. This value coincides with the MOID used in Solar System studies. In principle, the best orbit is the one with the smallest MOID at the recorded impact time but it depends on the actual values of the impact parameters (the score, see below). The position of the planet can be used with or without taking into consideration the uncertainties pointed out above as this has only minor effects on the precision of the final solution as long as $\Delta t_{\rm impact}$ is less than a few minutes. In de la Fuente Marcos & de la Fuente Marcos (2013, 2014) only $\Delta f_{\rm p}$ was sampled; here, we adopt a similar strategy allowing an uncertainty in $f_{\rm p}$ equivalent to about 180 s (see Table 10, Appendix A). Using a resolution of about $2\farcs6$ for this first phase of the Monte Carlo sampling is generally sufficient to obtain robust candidate orbits after a few million trials.

Regarding the issue of time standards, $t_{\rm impact}$ is expressed as Coordinated Universal Time (UTC) which differs by no more than 0.9 s from Universal Time (UT). Therefore and within the accuracy limits of this research, UTC and UT are equivalent. However, orbital elements and Cartesian state vectors (in general, Solar System ephemerides) are computed in a different time standard, the Barycentric Dynamical Time (TDB). UTC is discontinuous as it drifts with the addition of each leap second, which occur roughly once a year; in sharp contrast, TDB is continuous (for an extensive review on this important issue see Eastman et al. 2010). The JPL Horizons On-Line Ephemeris System shows that the difference between the uniform TDB and the discontinuous UTC was +67.18 s on 2014 January 1. Taking into account this correction, the impact time in the REB is 2014 January 2 at 03:06:32 TDB and the one computed in Sect. 3 is 2014 January 2 at 02:50:43.63 TDB.

In general and given two orbits, our Monte Carlo algorithm discretizes both orbits (sampling in true anomaly) and computes the distance between each and every pair of points (one on each orbit) finding the minimum value. If the discretization is fine enough, that minimum distance matches the value of the MOID obtained by other techniques. The approach to compute the MOID followed here is perhaps far more time consuming than other available algorithms but makes no a priori assumptions and can be applied to arbitrary pairs of heliocentric orbits. It produces results that are consistent with those from other methods. Numerical routines to compute the MOID have been developed by Baluev & Kholshevnikov (2005), Gronchi (2005), Šegan et al. (2011) and Wiśniowski & Rickman (2013), among others. Gronchi's approach is widely regarded as the de facto standard for MOID computations (Wiśniowski & Rickman 2013).

To further constrain the orbit, the coordinates of the impact point on the planet for our trial orbit are computed as described in e.g. Montenbruck & Pfleger (2000). In computing the longitude of impact, $\lambda_{\rm impact}$, it is assumed that the MOID takes place when the object is directly overhead (is crossing the local meridian at the hypocentre). Under this approximation, the local sidereal time corresponds to the right ascension of the object and its declination is the latitude of impact, $\phi_{\rm impact}$. In other words and for the Earth, as the local hour angle is zero when the meteor is on the meridian, the longitude is the right ascension of the meteor at the MOID minus the Greenwich meridian sidereal time (positive east from the prime meridian). Including the coordinates of the impact point as constraints has only relatively minor influence on orbit determination, the main effect is in the inclination that may change by up to $\sim$4% (de la Fuente Marcos & de la Fuente Marcos 2014). This second stage of the Monte Carlo sampling applies a resolution of about $1''$ and produces relatively precise results after tens to hundreds of billion trials. In this phase, only a short arc of a few degrees is used for the test impact orbit.

Applying the above procedure and for a given orbit, both the minimum separation (with respect to the planet at impact time) and the geocentric coordinates of the point of minimum separation can be estimated. Here, the MOID is synonymous of true minimal approach distance because we are studying actual impact orbits. In general, a very small value of the MOID does not imply that the orbit will result in an impact because protective dynamical mechanisms, namely resonances, may be at work. The next step is using Monte Carlo to find the optimal orbit: the one that places the object closest to the planet at impact time and also the one that reproduces the coordinates of the impact point (hypocentre) on the planet. In order to do that, the set of orbital elements (a, e, i, Ω, and ω) of the incoming body is randomly sampled within fixed (assumed) ranges following a uniform (or normal) distribution; for each set, the procedure outlined above is repeated so the optimal orbit is eventually found. The use of uniformly distributed random numbers or Gaussian ones does not affect the quantitative outcome of the algorithm, but in this section we utilize a uniform distribution instead of a standard normal distribution because this speeds up the task of finding the optimal orbit. Neglecting gravitational focusing and in order to have a physical collision, the MOID must be < 0.00004336 AU (one Earth's radius, $R_{\rm E}$, in AU plus the characteristic thickness of the atmosphere, 115 km). In this context,

MOIDs $< 1\ R_{\rm E}$ are regarded as unphysical. This approach is, in principle, computationally expensive but makes very few a priori assumptions about the orbit under study and can be applied to cases where little or no astrometric information is available for the meteor. Within the context of massively parallel processing, our approach is inexpensive though. Our algorithm usually converges after exploring several billion (up to a few trillion) orbits. Seeking the optimal orbit can be automated using a feedback loop to accelerate convergence in real time based on the criterion used in de la Fuente Marcos & de la Fuente Marcos (2013).

A key ingredient in our algorithm is the procedure to decide when a candidate solution is better than other. Candidate solutions must be ranked based on how well they reproduce the observed impact parameters, i.e. they must be assigned a score. A robust choice to rank the computed candidate solutions is a combination of two bivariate Gaussian distributions: one for the actual impact and a second one for its location. In order to rank the impact time we use:

$$\beta = e^{-\frac{1}{2}\left[\left(\frac{d-d_{\rm impact}}{\sigma_{d_{\rm impact}}}\right)^2+\left(\frac{f_{\rm E}-f_{\rm E_{impact}}}{\sigma_{f_{\rm E_{impact}}}}\right)^2\right]}, \tag{2}$$

where d is the MOID of the test orbit in AU, $d_{\rm impact} = 0$ AU is the minimum possible MOID, $\sigma_{d_{\rm impact}}$ is assumed to be the radius of the Earth in AU, $f_{\rm E}$ is the value of Earth's true anomaly used in the computation, $f_{\rm E_{impact}}$ is the value of Earth's true anomaly at the impact time (see Table 10, Appendix A), and $\sigma_{f_{\rm E_{impact}}}$ is half the angle subtended by the Earth from the Sun ($0\overset{\circ}{.}00488$). We assume that there is no correlation between d and $f_{\rm E}$. However, the values of the impact time and Earth's true anomaly at that time are linearly correlated in the neighbourhood of the impact point; i.e. $f_{\rm E_{impact}}$ is a proxy for the impact time. If $\beta > 0.368$, a collision is possible. Our best solutions have $\beta > 0.9999$. The MOID can be used to compute the altitude above the ground if $R_{\rm E}$ is considered. The altitude above the surface of the Earth is in the range 0–115 km (upper atmosphere limit). As for the impact location we use:

$$\Psi = e^{-\frac{1}{2}\left[\left(\frac{\lambda-\lambda_{\rm impact}}{\sigma_{\lambda_{\rm impact}}}\right)^2+\left(\frac{\phi-\phi_{\rm impact}}{\sigma_{\phi_{\rm impact}}}\right)^2\right]}, \tag{3}$$

where λ and ϕ are the impact coordinates for a given test orbit (if $\beta > 0.368$), and $\sigma_{\lambda_{\rm impact}}$ and $\sigma_{\phi_{\rm impact}}$ are the standard deviations associated with $\lambda_{\rm impact}$ and $\phi_{\rm impact}$ supplied with the actual (observational) impact values. Again, we assume that there is no correlation between λ and ϕ, and our best solutions have $\Psi > 0.9999$. The use of $\sigma_{\lambda_{\rm impact}}$ and $\sigma_{\phi_{\rm impact}}$ implicitly inserts the direction of the local tangent (or its projection) into the calculations (see below).

Impact events are defined by a number of parameters. Observational parameters are specified by a mean value and a standard deviation or uncertainty; they are assumed to be independent. Numerical experiments generate virtual impacts, if successful. The parameters associated with a virtual impact must be checked against the observational values in order to decide if a given pre-impact orbit can reproduce them. An uncertainty model must be applied to rank the tested pre-impact orbits. For this purpose, we use a Gaussian uncertainty model with multidimensional relevance ranking metrics. Equations (2) and (3) let us assign a score to any given candidate solution. Assuming independence, the score can be computed as $\beta \times \Psi$. The higher the score, the better the orbit. Equations (2) and (3) provide a simple but useful estimate of the probability that a given candidate solution could reproduce the impact parameters. Reproducing the observed values of the impact parameters (and those of any other available observational data) is the primary goal of our approach. Similar techniques are used in other astronomical contexts; see e.g. sect. 4.2 in Scholz et al. (1999) or sect. 4 in Sariya & Yadav (2015). The probability of being able to reproduce the impact parameters is different from the probability of impact; a certain pre-impact orbit may have an associated impact probability virtually equal to 1 and still be unable to reproduce the impact parameters if, for instance, the timing deviates significantly from the recorded impact time ($\pm 9\sigma$). Here, we assume that the probability of impact is computed in the usual way or number of successes divided by number of trials.

Our geometric approach is implemented iteratively as some initial guess for the pre-impact orbit is made based on some a priori observational knowledge; the pre-impact orbit is improved by inspecting the reconstruction of the impact and its rank. The procedure is iterated until an optimal solution is found. At this point, one may wonder how reliable our approach could be and what its intrinsic limitations are. The orbital elements and therefore the position of the target planet at the time of impact are assumed to be well known; if the input data are reliable enough then the computed solution must be equally robust. The time of impact and the coordinates of the impact point are the observables used to constrain both the input data (the Earth's ephemerides in our case) and the eventual solution. If the time of impact and/or the coordinates of the impact point are uncertain or wrong, then the solution obtained will be equally unreliable or incorrect. The time of impact is by far the most critical parameter. In our present case, it is a very reasonable assumption to consider that the available observational data ($t_{\rm impact}$,

$\lambda_{\rm impact}$ and $\phi_{\rm impact}$) are sufficiently robust to produce an equally sound orbital solution.

If information on the pre-impact velocity of the object is available, it can be used to further refine the candidate orbital solution, again by iteration. The observational pre-impact speed is the velocity at atmospheric entry, $v_{\rm impact}$. As a by-product of our geometric reconstruction, we obtain the relative velocity at atmospheric entry neglecting the acceleration caused by the Earth's gravitational field; this is called the hyperbolic excess velocity, v_∞, or the characteristic geocentric velocity of the meteor's radiant, $v_{\rm g}$. The velocity at atmospheric entry and the hyperbolic excess velocity are linked by the expression

$$v_\infty^2 = v_{\rm impact}^2 - v_{\rm escape}^2 \,, \tag{4}$$

where $v_{\rm escape} \sim 11.2$ km s^{-1} is the Earth's escape velocity at atmospheric entry. Therefore, for any geometrically reconstructed pre-impact orbit, $v_{\rm impact}$ can be easily estimated in order to compare with the observational data, even if our geometric approach is entirely non-collisional. The amount v_∞ can also be interpreted as the velocity of the object relative to an assumed massless Earth. Although not standard in meteor astronomy, here we have followed the terminology discussed by Chodas and Blake.[5,6] In Ceplecha (1987), a classic work in meteor astronomy, v_∞ is the velocity of the meteoroid corrected for the atmospheric drag and referred to the entry point in the Earth's atmosphere, i.e. our $v_{\rm impact}$.

Our geometric approach works because, for an object orbiting around the Sun, it is always possible to find an instantaneous Keplerian orbit that fits its instantaneous position and during a close encounter the largest orbital changes take place during the time interval immediately after reaching the distance of closest approach. In principle, degenerate orbital solutions (two or more very different impact orbits being compatible with a given set of impact data) are possible, but additional observational information such as how the meteor was travelling across the sky (e.g. north to south) and velocity-related data should be sufficient to break any degeneracy unless the orbits are part of the same family (very similar orbital parameters). However, if the orbits are so similar they belong to the same meteoroid stream (see e.g. Jopek & Williams 2013; Schunová et al. 2014).

[5]http://neo.jpl.nasa.gov/risks/

[6]http://neo.jpl.nasa.gov/risks/a29075.html

4.2 Validation: the case of the Almahata Sitta event

The algorithm described above, in its simplest form, was tested in the case of the Almahata Sitta event caused by the meteoroid 2008 TC_3 (Jenniskens et al. 2009; Oszkiewicz et al. 2012) and it was found to be able to generate an orbital solution consistent with those from other authors (de la Fuente Marcos & de la Fuente Marcos 2013). Applying the modified algorithm that includes the location of the impact point we obtain: $a = 1.3085 \pm 0.0003$ AU, $e = 0.3124 \pm 0.0002$, $i = 2\overset{\circ}{.}525 \pm 0\overset{\circ}{.}002$, $\Omega = 194\overset{\circ}{.}10618 \pm 0\overset{\circ}{.}00007$, $\omega = 234\overset{\circ}{.}466 \pm 0\overset{\circ}{.}008$ and $M = 330\overset{\circ}{.}840 \pm 0\overset{\circ}{.}013$, with $\lambda_{\rm impact} = 31\overset{\circ}{.}37 \pm 0\overset{\circ}{.}04$, $\phi_{\rm impact} = +20\overset{\circ}{.}87 \pm 0\overset{\circ}{.}06$ at an altitude of 27±20 km on 2008 October 07 02:45:40±5 UTC (at the time of the Almahata Sitta event the difference between TDB and UTC was +65.18 s). These are the average values of 11 best solutions ranked using Eqs. (2) and (3). In this and subsequent calculations the errors quoted correspond to one standard deviation (1σ) computed applying the usual expressions (see e.g. Wall & Jenkins 2012). The relative differences between this geometric orbital solution and the one computed by Steven R. Chesley, and available from the JPL Small-Body Database, are: 0.023% in a, 0.11% in e, 0.68% in i, 0.0026% in Ω, 0.0073% in ω, and 0.0026% in M. Therefore, the orbital solution has relatively small uncertainties when compared against a known robust determination. The values of the impact parameters are consistent with those available from the JPL.[7,8]

4.3 The most probable pre-impact orbit of 2014 AA in a strict geometric sense

We have applied the procedure described above using, as input, data from Table 10 (epoch 2456659.629537) and the coordinates of the impact point as given in Chesley et al. (2015). Figure 2 shows a representative sample (10^7 points) of our results as well as the best solution (red/black squares). Our best solution, found after about 10^{10} trials, appears in Table 3 (left-hand column) and produces a virtual impact at ($\lambda_{\rm impact}$, $\phi_{\rm impact}$, $t_{\rm impact}$) = ($-43\overset{\circ}{.}417 \pm 0\overset{\circ}{.}007$, $+14\overset{\circ}{.}632 \pm 0\overset{\circ}{.}008$, 2456659.62954±0.00002 JD TDB or 2014 January 2 at 3:05:25 UTC). From the MOID, the altitude is 47±31 km. The orbital solution displayed in Table 3, left-hand column, is the average of 15 representative good solutions ranked using Eqs. (2) and (3). The geometric impact probability for this orbital solution is virtually 1, given the very large number of trials. Two values of

[7]http://neo.jpl.nasa.gov/fireballs/

[8]http://neo.jpl.nasa.gov/news/2008tc3.html

τ are provided because it is customary to quote the τ closest to the epoch under study but it is also true that, as a result of the impact, 2014 AA never reached the 2456703.79 JD TDB perihelion so the previous one is also given for consistency.

Using the new determination presented in Sect. 3 and consistent data analogous to those in Table 10, we obtain (see Table 3, right-hand column): $a = 1.168706$ AU, $e = 0.216553$, $i = 1\overset{\circ}{.}36251$, $\Omega = 101\overset{\circ}{.}50175$, $\omega = 52\overset{\circ}{.}1144$, and $M = 325\overset{\circ}{.}5325$. This is the average of 27 representative good solutions. The virtual impact is now at ($\lambda_{\rm impact}$, $\phi_{\rm impact}$, $t_{\rm impact}$) = ($-43\overset{\circ}{.}714\pm0\overset{\circ}{.}008$, $+11\overset{\circ}{.}218\pm0\overset{\circ}{.}007$, 2456659.61856±0.00002 JD TDB or 2014 January 2 at 2:49:36.5 UTC); the altitude is 39±26 km. As for the entry velocity, the value obtained in Chesley et al. (2015) is 12.23 km s^{-1}; the $v_{\rm impact}$ from our geometric approach —see Eq. (4)— is 12.33 km s^{-1}.

Our approach provides the most probable solution, in a strict geometric sense, for the pre-impact orbit of 2014 AA. This solution is fully consistent with those in Table 1 even if no astrometry has been used to perform the computations. The high degree of coherence between the orbital elements derived using actual observations and those produced following the methodology described in this section clearly vindicates this geometric Monte Carlo approach as a valid method to compute low-precision —but still reliable— pre-impact orbits of the parent bodies of meteors. The values of the errors quoted represent the standard deviations associated with the selected sample of best orbits, they do not include the larger, systematic component linked to the observational values of impact coordinates and time (see above) that in the case of 2014 AA is dominant. It is true that the orbital solutions in Table 1 are rather uncertain, but in the case of 2008 TC_3 —which is much better constrained, including the values of the impact parameters— our approach also provides very good agreement with astrometry-based solutions (see de la Fuente Marcos & de la Fuente Marcos 2013 and above).

5 Pre-impact orbit: *N*-body approach

It can be argued that the Monte Carlo technique used in the previous section may not be adequate to make a proper determination of the pre-impact orbit of the parent body of an observed meteor. In particular, one may say that the use of two two-body orbits is absolutely inappropriate for this problem as three-body effects are fundamental in shaping the relative dynamics during the close encounter that leads to the impact. Let us assume that this concern is warranted.

5.1 A full *N*-body approach

In absence of astrometry, the obvious and most simple (but very expensive in terms of computing time) alternative to the method used in the previous section is to select some reference epoch (preceding the impact time), assume a set of orbital elements (a, e, i, Ω, ω, and τ), generate a Cartesian state vector for the assumed orbit at the reference epoch, and use N-body calculations to study the orbital evolution of the assumed orbit until an impact or a miss, within a specified time frame, occurs. If enough orbits are studied, the best pre-impact orbit can be determined. This assumption is based on the widely accepted notion that statistical results of an ensemble of collisional N-body simulations are accurate, even though individual simulations are not (see e.g. Boekholt & Portegies Zwart 2015). Given the fact that N-body simulations are far more CPU time consuming than the calculations described in the previous section, having a rough estimate of the orbital solution is essential to make this approach feasible in terms of computing time. The geometric Monte Carlo approach described above is an obvious candidate to supply an initial estimate for the orbit under study.

The method just described corresponds to that of an inverse problem where the model inputs (the pre-impact orbit) are unknown while the model outputs (the impact parameters) are known (see e.g. Press et al. 2007). Our simulation-optimization approach searches for the best inputs from among all the possible ones without explicitly evaluating all of them. We seek an optimal solution —fitting the data or model outputs within given constraints— and also enforce that the resulting data fit within certain tolerances, given by data uncertainties (those of the original, observational data). Our simulation model (the N-body calculations) is coupled with optimization techniques —based on Gaussian distributions analogous to Eqs. (2) and (3), see above— to determine the model inputs that best represent the observed data in an iterative process. The observational data are noisy (have errors) and the uncertainty is incorporated into the optimization (via the Gaussian distributions), but we also deal with the uncertainty by analysing multiple incarnations of the model inputs. Our hybrid optimization implementation maximizes the number of successful trials resulting from a Monte Carlo simulation. Our best solutions have scores > 0.9999 (see the discussion in Sect. 4.1).

The procedure described in this section can be seen as an inverse implementation of the techniques explored in Sitarski (1998, 1999, 2006). In these works, the author investigates the conditions for a hypothetical collision of a minor planet with the Earth creating sets of

Table 3 Heliocentric Keplerian orbital elements of 2014 AA from our geometric approach. Values include the 1σ uncertainty. The orbit is computed at an epoch arbitrarily close to the impact time. The two values quoted for τ are separated by one full orbital period. The orbit on the left-hand column produces a virtual impact with parameters consistent with those used in Chesley et al. (2015) or Farnocchia et al. (2016), the orbit in the right-hand column is consistent with the new determination presented in Sect. 3 (see the text for details).

Semi-major axis, a (AU)	=	1.16995±0.00009	1.168706±0.000010
Eccentricity, e	=	0.21763±0.00008	0.216553±0.000008
Inclination, i (°)	=	1.4319±0.0002	1.36251±0.00006
Longitude of the ascending node, Ω (°)	=	101.50618±0.00003	101.50175±0.00003
Argument of perihelion, ω (°)	=	52.1249±0.0005	52.1144±0.0002
Mean anomaly, M (°)	=	325.609±0.006	325.5325±0.0006
Time of perihelion passage, τ (JD TDB)	=	2456241.57±0.06	2456242.327±0.006
		2012-Nov-10 01:39:21.6 UTC	2012-Nov-10 19:49:26.4 UTC
	=	or 2456703.79	or 2456703.802
		2014-Feb-15 06:56:09.6 UTC	2014-Feb-15 07:13:26.4 UTC
Perihelion, q (AU)	=	0.91534±0.00002	0.915619±0.000002
Aphelion, Q (AU)	=	1.4246±0.0002	1.42179±0.00002

Fig. 1 Hypocentre location of the 2014 AA event on the surface of the Earth (red star and error ellipse) as given in Table 2 and assuming specific source properties (see the text for details). The previous REB determination (yellow star and error ellipse), and the locations and codes of the three detecting stations are also displayed. The error ellipses show the 90th percentile; the estimated directions of arrival (back-azimuth) are displayed for each infrasound station (green lines).

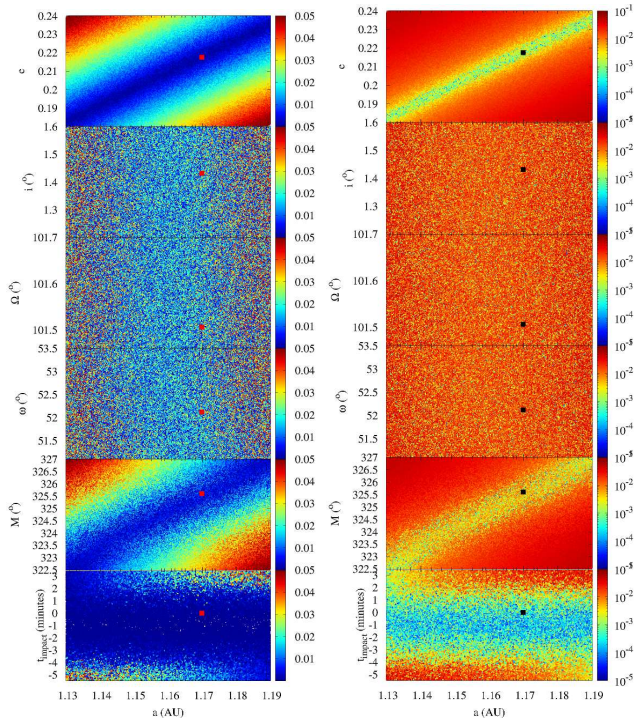

Fig. 2 Results from the geometric approach described in the text for the 2014 AA impactor. The colours in the colour maps are proportional to the value of the minimal approach distance in AU for a given test orbit following the associated colour box (linear scale, left-hand panels; logarithmic scale, right-hand panels). Only test orbits with MOIDs under 0.05 AU are displayed; the solution in Table 3 (left-hand column) is also indicated (red/black squares). A representative sample of 10^7 test orbits is plotted. In this figure, $t_{\rm impact}$ is referred to the epoch JD TDB 2456659.629537, the one used in Chesley et al. (2015) and Farnocchia et al. (2016).

artificial observations with the objective of finding out the time-scales necessary to realise that a collision is unavoidable and to determine a precise impact area on the Earth's surface. In his work, the emphasis is made in how the uncertainties in the observations affect our ability to be certain of an impending collision and, in the case of a confirmed one, to be able to compute the correct impact location. In our case, we assume that (at least initially) no pre-impact observations are available, only the impact parameters are known. Sitarski's study uses the pre-impact information as input to develop his methodology, but here we use the post-impact data as a starting point. Sitarski's work is an example of solving a forward problem, ours of solving an inverse problem. The use of impact data to improve orbit solutions is not a new concept, it was first used by Chodas & Yeomans (1996) in the orbit determination of 16 of the fragments of comet Shoemaker-Levy 9 that collided with Jupiter in July 1994.

It may be argued that the type of inverse problem studied here (going from impact to orbit) has a multiplicity of solutions as we seek six unknowns (the orbital parameters) and the impact parameters are only three ($t_{\rm impact}$, $\lambda_{\rm impact}$ and $\phi_{\rm impact}$, but also $h_{\rm impact}$). In general, the solution to an inverse problem may not exist, be non-unique, or unstable. However, it is a well known fact used in probabilistic curve reconstruction (see e.g. Unnikrishnan et al. 2010) that if a curve is smooth, the data scatter matrix (that contains the values of the variances) will be elongated and that its major axis, or principal eigenvector, will approximate the direction of the local tangent. It is reasonable to assume that the pre-impact orbit of the parent body of a meteor in the neighbourhood of the impact point —high in the atmosphere— is smooth and therefore that the dispersions in $\lambda_{\rm impact}$, $\phi_{\rm impact}$, and $h_{\rm impact}$ (supplied with their values) provide a suitable approximation to the local tangent as the principal eigenvector of the data scatter matrix is aligned with the true tangent to the impact curve. In this context and by using the values of the dispersions (as part of the candidate solution ranking process, see above), we have indirect access to the direction of the instantaneous velocity and perhaps its value. In any case, if $v_{\rm impact}$ is available the solution of the inverse problem is unique (for additional details, see de la Fuente Marcos et al. 2015).

In this section we implement and apply an N-body approach to solve the problem of finding the pre-impact orbit of the parent body of a meteor. This approach is applied within a certain physical model. Our model Solar System includes the perturbations by the eight major planets and treats the Earth and the Moon as two separate objects; it also incorporates the barycentre of the dwarf planet Pluto–Charon system and the three most massive asteroids of the main belt, namely, (1) Ceres, (2) Pallas, and (4) Vesta. Input data are reference epoch and initial conditions for the physical model at that epoch. We use initial conditions (positions and velocities referred to the barycentre of the Solar System) provided by the JPL HORIZONS[9] system (Giorgini et al. 1996; Standish 1998; Giorgini & Yeomans 1999; Giorgini et al. 2001) and relative to the JD TDB (Julian Date, Barycentric Dynamical Time) 2456658.628472222 epoch which is the $t = 0$ instant (see Table 11, Appendix B); in other words, the integrations are started ∼24 h before $t_{\rm impact}$.

The N-body simulations performed here were completed using a code that implements the Hermite integration scheme (Makino 1991; Aarseth 2003). The standard version of this direct N-body code is publicly available from the IoA web site.[10] Relative errors in the total energy are as low as 10^{-14} to 10^{-13} or lower. The relative error of the total angular momentum is several orders of magnitude smaller. The systematic difference at the end of the integration, between our ephemerides and those provided by the JPL for the Earth, is about 1 km. As the average orbital speed of our planet is 29.78 km s^{-1}, it implies that the temporal systematic error in our virtual impact calculations could be as small as 0.04 s. Non-gravitational forces, relativistic and oblateness terms are not included in the simulations, additional details can be found in de la Fuente Marcos & de la Fuente Marcos (2012). The Yarkovsky and Yarkovsky–O'Keefe–Radzievskii–Paddack (YORP) effects (see e.g. Bottke et al. 2006) may be unimportant when objects are tumbling or in chaotic rotation —but see the discussion in Vokrouhlický et al. (2015) for 99942 Apophis (2004 MN_4)— as it could be the case of asteroidal fragments. Relativistic effects, resulting from the theory of general relativity are insignificant when studying the long-term dynamical evolution of minor bodies that do not cross the innermost part of the Solar System (see e.g. Benitez & Gallardo 2008). For a case like the one studied here, the role of the Earth's oblateness is rather negligible —see the analysis in Dmitriev et al. (2015) for the Chelyabinsk superbolide. The effect of the atmosphere is not included in the calculations as we are interested in the dynamical evolution prior to the airburst event. For the particular case of the Chelyabinsk superbolide, table S1 in Popova et al. (2013) shows that the value of the apparent velocity of the superbolide remained fairly constant between the altitudes of 97.1 and 27 km. This fact can be used to argue that neglecting the influence of the atmosphere should not have any adverse effects on the results of our analysis.

[9] http://ssd.jpl.nasa.gov/?horizons

[10] http://www.ast.cam.ac.uk/~sverre/web/pages/nbody.htm

5.2 Zeroing in on the best orbital solution

The actual implementation of the ideas outlined above is simple:

1. A Monte Carlo approach is used to generate sets of orbital elements. In this case, Gaussian random numbers are utilized to better match the results of astrometry-based solutions; the Box-Muller method (Box & Muller 1958; Press et al. 2007) is applied to generate random numbers with a normal distribution.
2. For each set of orbital parameters, the Cartesian state vector is computed at $t = 0$.
3. An N-body simulation is launched as described above, running from the JD TDB 2456658.628472222 epoch until JD TDB 2456660.82.
4. The output is processed to check for an impact or a miss.
5. If an impact takes place, the impact time and the location of the impact point are recorded; the coordinates of the impact point are computed as described in the previous section. The altitude above the surface of the Earth is in the range 0–115 km (upper atmosphere limit). This is consistent with infrasound propagation; in general, airbursts observed by global infrasound sensors occur below or around the stratosphere (ground up to 60–65 km).
6. If a miss, the value of the minimal approach distance is recorded for statistical purposes.
7. Candidate impact solutions are ranked using expressions similar to Eqs. (2) and (3) and assigned a score.
8. As the score improves, the new sets of orbital elements generated in step #1 are based on the newest best solution in order to speed up convergence towards the optimal orbital determination, further improving the score of the subsequent candidate solutions.

A large number of test orbits is studied. The volume of orbital parameter space explored by the algorithm is progressively reduced as the optimal solution is approached. In general, the data output interval is nearly 5 s; therefore, the impact is properly resolved in terms of time and space. At the typical impact speeds induced here ($\sim$12 km s^{-1}) an object travels the Earth's diameter in over 17 minutes and crosses the atmosphere in less than 10 s.

The orbital elements of our test orbits are varied randomly, within the ranges defined by their mean values and standard deviations. They represent a number of different virtual impactors moving in similar orbits, they do not attempt to incarnate a set of observations obtained for a single impactor. If actual observations are utilized, we have to consider how the elements affect each other using the covariance matrix or following the procedure described in Sitarski (1998, 1999, 2006). Due to the large uncertainties affecting the orbit of 2014 AA, we decided to neglect any corrections based on the covariance matrix to generate our test or control orbits at this stage but see Sect. 8.2. This arbitrary choice should not have any major effects on the assessment of the orbits made here.

We have performed an initial search for an optimal orbit using the N-body approach and the solution from the previous section (Table 3, left-hand column) assuming a normal distribution in orbital parameters. In this case, the probability of impact is $\leq$0.043. The virtual impacts take place 30 minutes to 3 h earlier than the time resulting from the analysis of infrasounds in Chesley et al. (2015) or Farnocchia et al. (2016), the longitude of impact has a range of nearly 180°centred at about −28°, and the latitude is in the range (−11, 30)°centred at about 9°. Using the solution in Table 3, right-hand column, the probability of impact is 0.455, the recorded impact time is 102±42 minutes earlier than the one given in Table 2, the longitude of impact has a range close to 180°centred at about −51°, and the latitude is in the range (−5, 18)°centred at 10°. These results confirm that the approach discussed in the previous section is able to produce reasonably correct low-precision pre-impact orbits of meteors. In theory, the full N-body approach is capable of returning orbital determinations matching those from classical methods in terms of precision.

Using the impact parameters based on infrasound data as described in Chesley et al. (2015) or Farnocchia et al. (2016) and after a few million trials, mostly automated, we find the solution displayed in Table 4, left-hand column, that is referred to epoch JD TDB 2456658.628472222. It is the average of 23 good solutions ranked as explained above (score > 0.9999). The altitude above the surface of the Earth at impact was 60±14 km. For this solution, the geocentric value of the entry velocity is 12.186±0.011 km s^{-1} which is reasonably consistent with that in Chesley et al. (2015), 12.23 km s^{-1}, and also with the one in Farnocchia et al. (2016), 12.17 km s^{-1}. We consider that the orbit displayed in Table 4 (left-hand column) is the most probable pre-impact orbit of 2014 AA if the impact parameters in Chesley et al. (2015) or Farnocchia et al. (2016) are assumed, and if the available astrometry is neglected. Figure 3 shows the results of an N-body experiment including 10^5 test orbits resulting from a Monte Carlo simulation with a normal distribution in orbital parameters according to Table 4, left-hand column. In this experiment, the probability of impact is >0.99999. The rather coarse distribution in impact

Table 4 Heliocentric Keplerian orbital elements of 2014 AA from our N-body approach if the impact parameters in Chesley et al. (2015) or Farnocchia et al. (2016) are assumed (left-hand column) and for the new impact solution presented in Sect. 3 (right-hand column). Values include the 1σ uncertainty. The orbits are computed at epoch JD TDB 2456658.628472222 that corresponds to 03:03:52.82 UTC on 2014 January 1, J2000.0 ecliptic and equinox.

Semi-major axis, a (AU)	=	1.1639272±0.0000003	1.1621932±0.0000004
Eccentricity, e	=	0.2136664±0.0000003	0.2115415±0.0000004
Inclination, i (°)	=	1.46070±0.00006	1.38009±0.00006
Longitude of the ascending node, Ω (°)	=	101.59934±0.00002	101.60617±0.00004
Argument of perihelion, ω (°)	=	52.58912±0.00003	52.34221±0.00006
Mean anomaly, M (°)	=	324.124173±0.000013	324.14040±0.00002
Time of perihelion passage, τ (JD TDB)	=	2456704.335877±0.000005	2456704.213146±0.000005
Perihelion, q (AU)	=	0.91523502±0.00000010	0.9163412±0.0000002
Aphelion, Q (AU)	=	1.4126194±0.0000007	1.4080453±0.0000009
Impact time, $t_{\rm impact}$ (JD UTC)	=	2456659.62878±0.00003	2456659.61773±0.00004
Longitude of impact, $\lambda_{\rm impact}$ (°)	=	−43.425±0.010	−43.704±0.007
Latitude of impact, $\phi_{\rm impact}$ (°)	=	+14.630±0.003	+11.228±0.014

time is the result of the unavoidable discretization of the output interval that also has an effect on the distribution in altitude (not shown). When computers are used to produce a uniform random variable —i.e. to seed the Box-Muller method to generate random numbers from the standard normal distribution with mean 0 and standard deviation 1— it will inevitably have some inaccuracies because there is a lower boundary on how close numbers can be to 0. For a 64 bits computer the smallest non-zero number is 2^{-64} which means that the Box-Muller method will not produce random variables more than 9.42 standard deviations from the mean.

If the impact parameters presented in Sect. 3 are used instead of the values in Chesley et al. (2015) or Farnocchia et al. (2016), a slightly different solution is obtained, see Table 4, right-hand column. This orbital determination is the average of 20 good solutions. For this solution, the value of the entry velocity is 12.172±0.008 km s^{-1} at an altitude above the surface of the Earth at impact of 41±10 km.

5.3 Improving the solution using astrometry

It may be argued that, for the particular case of 2014 AA, the astrometry is a piece of information far too important to be neglected as we summarily did in the previous section. The MPC Database[11] includes seven astrometric observations; the JPL Small-Body Database computed its current solution using the same seven astrometric positions and one derived from infrasound data. Until 2015 April 13 00:35:03 UT, the JPL computed its solution using only the seven astrometric positions (see Table 1). The seven observations from the MPC were published in Kowalski et al. (2014) and they are topocentric values (see Table 6).

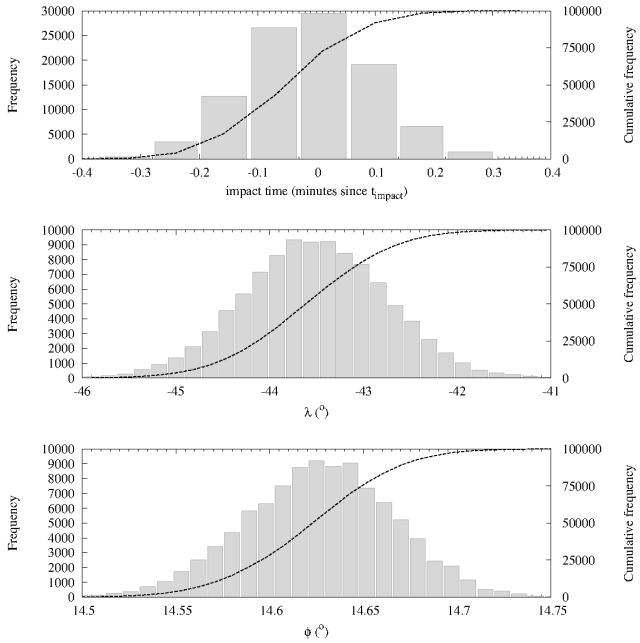

Fig. 3 Resulting distributions in impact parameter space for an experiment using our initial solution from the N-body approach (see Table 4, left-hand column). The impact time is referred to the value based on infrasound data according to Chesley et al. (2015) or Farnocchia et al. (2016); the rather coarse distribution in impact time is induced by our data output interval of nearly 5 s.

[11] http://www.minorplanetcenter.net/db_search

Simulations provide geocentric equatorial coordinates directly. Observational topocentric values can be transformed into geocentric values, but the conversion process is rather uncertain because the value of the geocentric distance associated with each pair of topocentric equatorial coordinates is, in principle, unknown unless we adopt an orbital solution. Uncertainties in the plane of sky as seen from the geocentre can be large, perhaps as large as 40″ (=0°.011=0$^{\rm h}$.00074). The other option, going from the values of the geocentric equatorial coordinates obtained from simulations to topocentric values, is in theory less prone to error. Unfortunately, high precision (deviations of a few arcseconds or smaller) conversion from geocentric equatorial coordinates to topocentric is not exempt of problems itself when the values of the geocentric distance are as small as the ones considered here.

Formulae dealing with the conversion of the position of a body on the celestial sphere as viewed from the Earth's centre to the one seen from a location on the surface of our planet of known longitude, latitude and altitude (parallax in right ascension and declination) have been discussed in e.g. Maxwell (1932) or Smart (1977). These expressions depend on the value of the Greenwich Mean Sidereal Time at 0 h UTC and also on the model used to describe the shape of the Earth. The conversion algorithm used to compute the root-mean-square deviation in order to compare differences between the values of the topocentric (for observatory code G96, Mt. Lemmon Survey) equatorial coordinates derived from simulations and those from observations has been validated/calibrated using MPC data and, for the range of geocentric distances of interest here, it has been found to introduce systematic errors <1″ in both right ascension and declination; for geocentric distances >0.1 AU the systematic errors are completely negligible. The original topocentric values given in Kowalski et al. (2014) are apparent values; they give us the position of 2014 AA when its light left the asteroid. Geocentric equatorial coordinates derived from simulations give the true values of these coordinates. However, our values can be adjusted for light-time, i.e. they can be made apparent values. The computed position will be observed at a later time, $t_{\rm i} + \Delta_{\rm i}/c$, where $t_{\rm i}$ is the time when the light was reflected, $\Delta_{\rm i}$ is the asteroid–Earth distance, and c is the speed of light. For the range of distances associated with the available observations, the epoch correction is $\sim$ 1.35 s, that is small enough to be neglected.

Figure 4 shows the evolution of the topocentric equatorial coordinates (right ascension, α, and declination, δ) during the integrations for three orbital solutions, including the two derived in the previous section —see

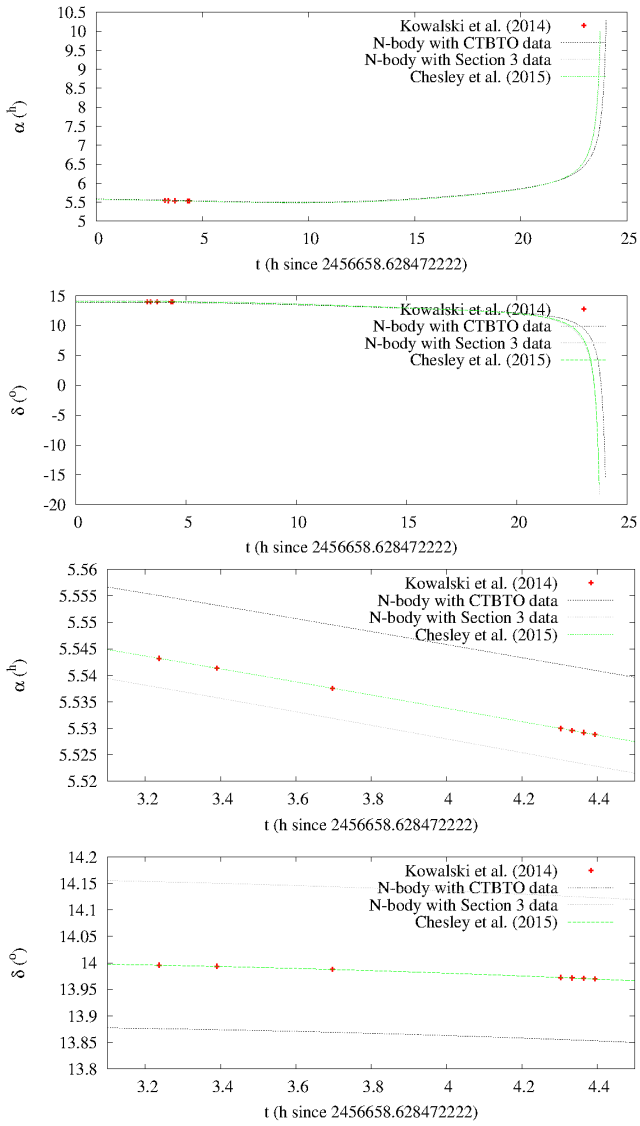

Fig. 4 Time evolution of the topocentric equatorial coordinates for the various candidate orbital solutions of 2014 AA. The entire integration is displayed on the first two panels and the time window defined by the observations in Kowalski et al. (2014) is displayed on the other two (see the text for details).

Table 4, left-hand column, labelled as 'N-body with CTBTO data' and right-hand column, labelled as 'N-body with Section 3 data'— and that discussed in Chesley et al. (2015). The orbital determinations labelled as 'N-body with CTBTO data' and 'Chesley et al. (2015)' are based on the same values of the impact parameters, but the one in Chesley et al. (2015) was refined using the available astrometry. The first two panels show the entire time evolution and the other two are restricted to the time window defined by the observations in Kowalski et al. (2014); the actual observations are also displayed, their associated error bars are too small to be seen. The limitations of our impact-parameters-only N-body determinations are clear from the figure, but the fact is that —in the vast majority of cases— meteoroid impacts do not have any associated pre-impact astrometry. For those cases, the methodologies presented in this research could be very helpful for both finding pre-impact orbital solutions and assessing the quality of the ones obtained using other, more classical techniques.

In this section we improve our solutions considering the available astrometry. In order to achieve this goal, we have used a bivariate Gaussian distribution to minimize the deviations between the values of the topocentric coordinates resulting from our candidate orbital solution and the values of the topocentric equatorial coordinates in Kowalski et al. (2014). After a few million trials following the methodology explained above and enforcing consistency with the impact parameters presented in Sect. 3 within 1σ, we obtain the orbital solution displayed in Table 5 and plotted in Fig. 5 under the label 'N-body with astrometry'. It is only slightly different (the largest difference appears in the value of the orbital inclination) from the previous one (compare values in Table 5 against those in the right-hand column of Table 4) but matches the astrometry quite well. The root-mean-square deviation in α is $0\farcs59$ and the one in δ is $0\farcs28$.

The results from the current solution provided by the JPL Small-Body Database and presented in Farnocchia et al. (2016) are also displayed in Fig. 5 for comparison; this integration has been performed under the same framework (see Sect. 6.7 for details) as for all the other ones, but using a Cartesian state vector (as initial conditions) computed by the HORIZONS On-Line Ephemeris System. The two thinner curves, parallel to the one of our best solution, represent the upper and lower boundaries for the values of the topocentric equatorial coordinates of a sample of 1,000 orbits generated using the covariance matrix (see Sect. 8.2 for details) from our own orbital solution. The orbital solution displayed in Table 5 is therefore consistent with the available astrometry and consistent within 1σ of the values in Table 2, the mutual delay in impact time is about 15 minutes; in addition, the altitude of the virtual airburst is 47±4 km that is also consistent with the expectations from infrasound modelling.

Applying the same approach but using the impact parameters in Chesley et al. (2015) or Farnocchia et al. (2016) —the REB solution, see Sects. 2 and 3— as constraints, we could not find a solution able to comply with the astrometry within $1''$ rms and the impact solution within 1σ. It is numerically impossible to satisfy both requirements concurrently. This negative outcome is in agreement with the discussion in Chesley et al. (2015) or Farnocchia et al. (2016). The resulting virtual impact parameters in Chesley et al. (2015) or Farnocchia et al. (2016) are only consistent within 3σ of the values in the REB solution due to a significant offset in latitude (see e.g. fig. 1 in Farnocchia et al. 2016).

In Fig. 5, the curve labelled 'N-body with astrometry' is representative of those virtual impactors which are more consistent with the available astrometry, but still compatible with the improved impact parameters presented in Sect. 3 (within 1σ). They determine a volume in orbital parameter space about an orbit that goes evenly between the first and the last observations in Kowalski et al. (2014), this defines an eye-of-a-needle on the sky (see Fig. 6, top panel); any virtual impactor originated from that radiant will comply with the available astrometry to a certain degree (see Fig. 5) and it will hit the Earth with some values of the impact parameters consistent with the limits derived in Sect. 3 (see Fig. 6, bottom panel, and Fig. 7).

Figure 6 shows the results of three experiments consisting of 2×10^4 test orbits each. The top panel shows the true geocentric equatorial coordinates of the virtual impactors at the beginning of the simulation, i.e. at epoch 2456658.628472222 JD TDB. The points in red correspond to test orbits within 1σ of the orbital solution in Table 5, those in blue have a 10σ spread, and the green ones have 30σ. However, the points have been generated using uniformly distributed random numbers in order to survey the relevant region of the orbital parameter space evenly. Each virtual impactor generates one point on the bottom panel of the figure following the same colour pattern. The impact point derived from the infrasound data as described in Chesley et al. (2015) and the one presented in Sect. 3 are also plotted with error bars. If the virtual impactors are forced to pass through the astrometry, the simulated impacts are fully statistically consistent —in terms of coordinates— with the determination based on infrasound data presented in Sect. 3 but only marginally consistent with the one used in Chesley et al. (2015) due to the values of the

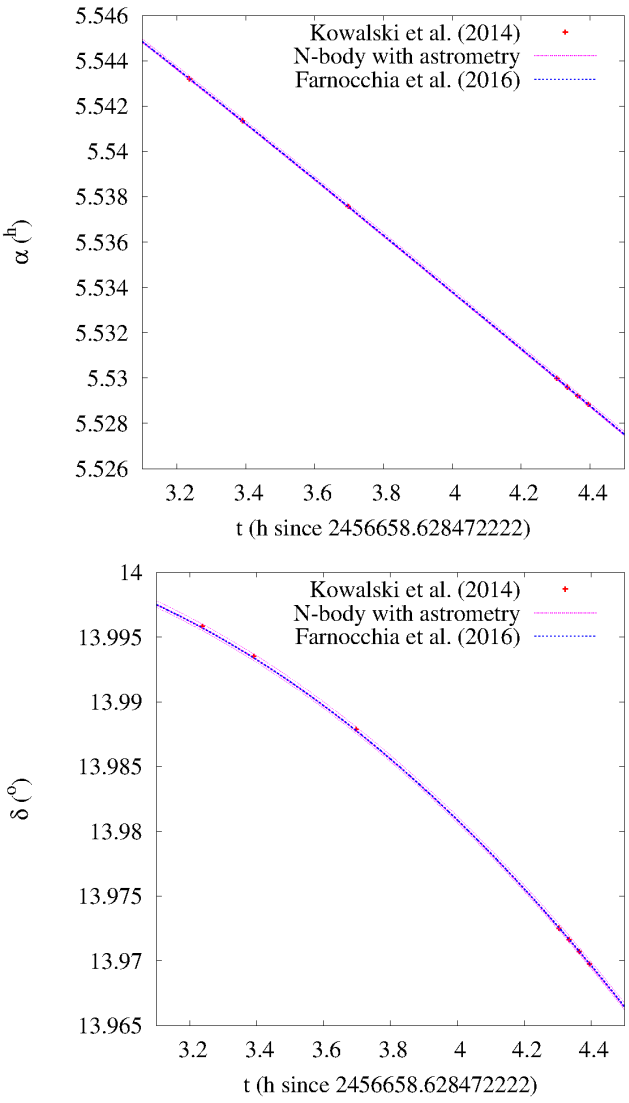

Fig. 5 Time evolution of the topocentric equatorial coordinates during the time window defined by the observations in Kowalski et al. (2014). A relevant integration with a root-mean-square deviation in α of 0.″6 and 0.″3 in δ with respect to the values in Kowalski et al. (2014) is labelled 'N-body with astrometry', this solution (Table 5) is compatible with the improved impact parameters presented in Sect. 3 (within 1σ). The thinner curves parallel to it give the maximum and minimum values of the coordinates at the given time for a set of 1,000 control orbits generated from our favoured solution using the covariance matrix (see Sect. 8.2).

Table 5 Same as Table 4 but considering the available astrometry. The evolution of the best orbital determination presented here matches (within 1σ) the impact parameters in the new impact solution presented in Sect. 3. There is no best solution matching (within 1σ) the impact parameters in Chesley et al. (2015) or Farnocchia et al. (2016), such solution cannot be found.

Semi-major axis, a (AU)	= 1.1623128±0.0000002
Eccentricity, e	= 0.2116144±0.0000002
Inclination, i (°)	= 1.41559±0.00002
Longitude of the ascending node, Ω (°)	= 101.608626±0.000014
Argument of perihelion, ω (°)	= 52.33925±0.00003
Mean anomaly, M (°)	= 324.146021±0.000008
Time of perihelion passage, τ (JD TDB)	= 2456704.213037±0.000004
Perihelion, q (AU)	= 0.91635067±0.00000013
Aphelion, Q (AU)	= 1.4082749±0.0000005
Impact time, $t_{\rm impact}$ (JD UTC)	= 2456659.62830±0.00002
Longitude of impact, $\lambda_{\rm impact}$ (°)	= −44.663±0.013
Latitude of impact, $\phi_{\rm impact}$ (°)	= +13.057±0.006

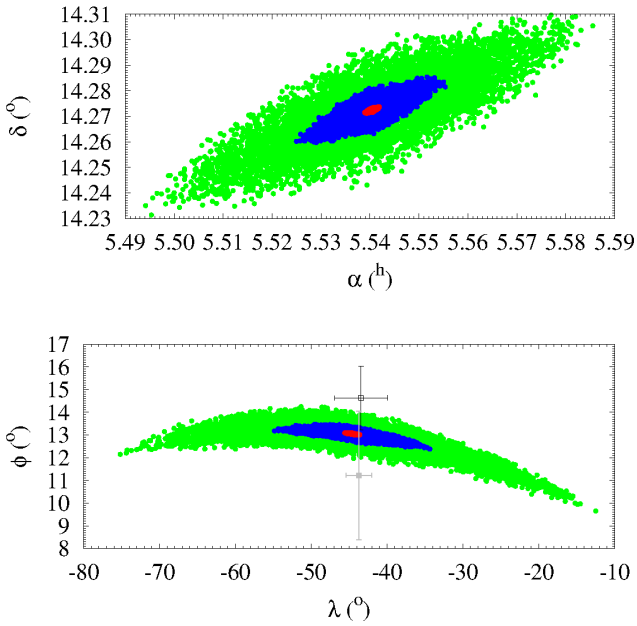

Fig. 6 True radiant geocentric equatorial coordinates (top panel) and their associated virtual impact coordinates (bottom panel). Virtual impacts plotted in green represent those associated with sets of orbital elements within 30σ of the orbital solution in Table 5, those in blue are the result of a 10σ spread, and the ones in red are restricted to 1σ. The impact point derived from the infrasound data in Chesley et al. (2015) appears in black with its approximate error bars, our determination presented in Sect. 3 is plotted in grey.

latitude which are too far south with respect to that from the REB. This fact clearly shows why our method failed to find a solution able to comply with the astrometry within $1''$ rms and the REB solution within 1σ, it is numerically impossible.

The distribution on the surface of the Earth of the virtual impacts studied here is more clearly displayed in Fig. 7 where the virtual impacts define an arc extending from the Caribbean Sea to West Africa if deviations as large as 30σ from the orbital solution in Table 5 are allowed. Figure 7 also displays the path of risk (the projection of the trajectory of the incoming body on the surface of the Earth as it rotates) associated with a representative most probable solution (see Fig. 5). The object was easily observable from Arizona 20 h before impact; the path has been stopped nearly at the time of impact.

Figures 8 and 9 show the results of the same three experiments described above in terms of the impact time. Those virtual impactors strictly compatible with the astrometry define a very small range for the associated impact time. The value of the impact time derived from infrasound data in Sect. 3 is compatible with virtual impactors from the region consistent with the astrometry. Figure 9 shows the three pieces of information together and the statistical consistency is quite obvious. The ranges in $v_{\rm g}$ and $v_{\rm impact}$ are plotted in Fig. 10. There are no known meteor showers with parameters similar to those in Figs. 8 and 10 (see e.g. Jenniskens 2006 or the most up-to-date information in Jopek & Kanuchová 2014), but the value of $v_{\rm g}$ is rather low to be easily detectable if they do exist. The coordinates of the radiant associated with the orbital solution in Table 5 are $\alpha_0 = 5\overset{\rm h}{.}540281 \pm 0\overset{\rm h}{.}000003$ ($83\overset{\circ}{.}10421 \pm 0\overset{\circ}{.}00004$) and $\delta_0 = +14\overset{\circ}{.}27232 \pm 0\overset{\circ}{.}00005$; the values of the velocities are $v_{\rm impact} = 12.170 \pm 0.003$ km s^{-1} and $v_{\rm g} = 5.0589 \pm 0.0001$ km s^{-1}.

These results give a clear picture on how precise an orbital solution should be in order to generate reliable impact predictions in terms of timing and location. We consider that the orbit in Table 5 is the best possible and the one that we regard as the most probable pre-impact orbit of 2014 AA because it matches the available astrometry reasonably well, its associated virtual impacts are consistent with the impact solution found using infrasound data in Sect. 3, and it has been computed for an epoch sufficiently distant from the impact time to give an accurate orbital solution, appropriate to study both the past dynamical evolution of 2014 AA and the possible existence of other objects moving in similar orbits among the known NEOs (see Sects. 7 and 8).

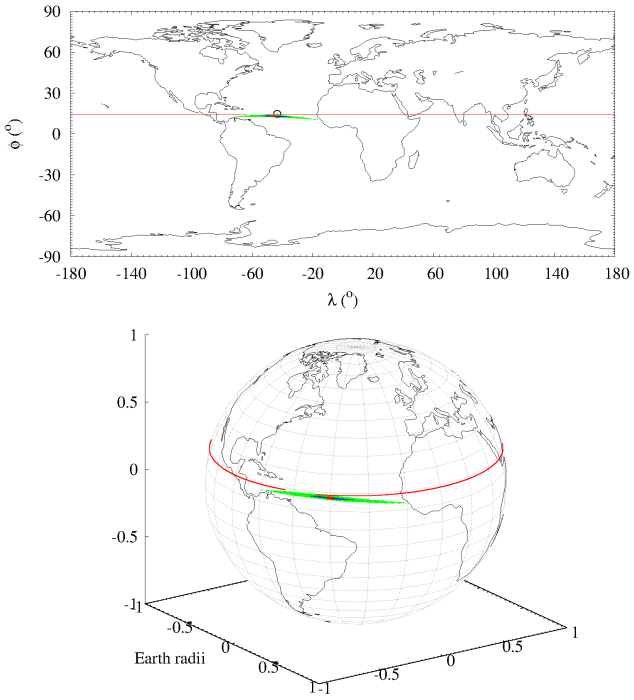

Fig. 7 Distribution on the surface of the Earth of the virtual impacts studied in Sect. 5.3. Virtual impactor colours are as in Fig. 6. The impact point derived from the infrasound data described in Chesley et al. (2015) appears as a circle. This figure is similar to panel b, fig. 5 in Sitarski (1998). The path of risk for one representative orbit is also displayed; it reached an altitude above the surface of the Earth of 47.80 km at coordinates ($44\overset{\circ}{.}81$ W, $13\overset{\circ}{.}02$ N). The red curve outlines the flight path (E to W) of the object; it starts above the Caribbean Sea. The location of the impact point as in Chesley et al. (2015) is also plotted. Only nearly 23 h prior to the strike are displayed.

Table 6 Comparison between the values of the topocentric (for observatory code G96, Mt. Lemmon Survey) and geocentric equatorial coordinates (R.A. in hh:mm:sec, Decl. in °:′:″) of 2014 AA computed from the solution provided by the MPC[1] and the one available from the JPL (Farnocchia et al. 2016). The original, observational (topocentric) values (Kowalski et al. 2014) are also displayed. (J2000.0 ecliptic and equinox. Sources: MPC and HORIZONS On-Line Ephemeris System.)

Source	Kowalski et al. (2014)		MPC				JPL			
	topocentric		geocentric		topocentric		geocentric		topocentric	
DATE UTC	R.A. (J2000)	Decl.	R.A. (J2000)	Decl.	R.A. (J2000)	Decl.	R.A. (J2000)	Decl.	R.A. (J2000)	Decl.
2014 01 01.26257	05:32:35.55	+13:59:45.0	05:32:39.4	+14:16:32	05:32:35.5	+13:59:45	05:32:39.34	+14:16:14.2	05:32:35.56	+13:59:45.0
2014 01 01.26896	05:32:28.89	+13:59:36.7	05:32:40.4	+14:16:32	05:32:28.8	+13:59:37	05:32:40.20	+14:16:13.9	05:32:28.87	+13:59:36.6
2014 01 01.28176	05:32:15.27	+13:59:16.4	05:32:42.4	+14:16:33	05:32:15.2	+13:59:17	05:32:41.95	+14:16:13.2	05:32:15.26	+13:59:16.2
2014 01 01.30701	05:31:47.92	+13:58:21.1	05:32:46.7	+14:16:34	05:31:47.9	+13:58:21	05:32:45.56	+14:16:12.0	05:31:47.92	+13:58:21.2
2014 01 01.30828	05:31:46.54	+13:58:17.9	05:32:46.9	+14:16:34	05:31:46.5	+13:58:18	05:32:45.75	+14:16:11.9	05:31:46.54	+13:58:17.9
2014 01 01.30955	05:31:45.15	+13:58:14.6	05:32:47.1	+14:16:34	05:31:45.1	+13:58:15	05:32:45.93	+14:16:11.8	05:31:45.15	+13:58:14.5
2014 01 01.31081	05:31:43.79	+13:58:11.1	05:32:47.3	+14:16:34	05:31:43.7	+13:58:11	05:32:46.12	+14:16:11.8	05:31:43.79	+13:58:11.2

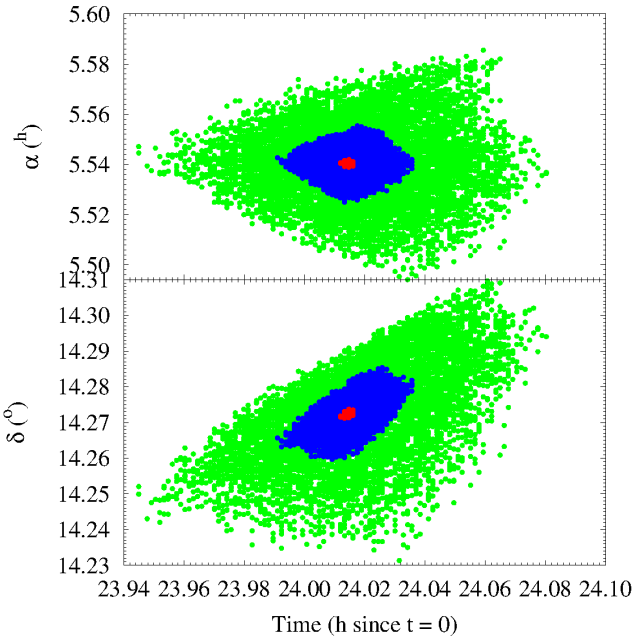

Fig. 8 True radiant geocentric equatorial coordinates of the virtual impactors as a function of the impact time. Virtual impactor colours as in Fig. 6.

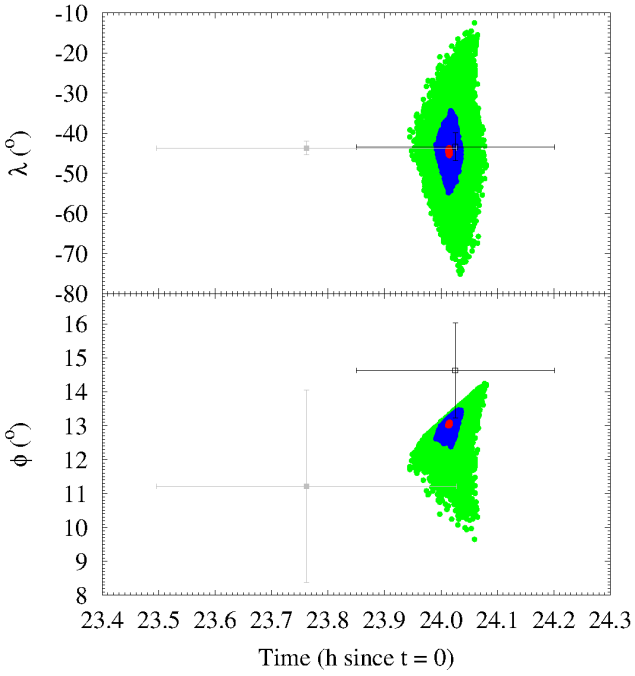

Fig. 9 Impact coordinates of the virtual impacts as a function of the impact time. Virtual impactor colours as in Fig. 6. The impact point derived from the infrasound data in Chesley et al. (2015) appears in black with error bars, our determination presented in Sect. 3 is plotted in grey.

6 Our results in context

Here and in order to place our results in context, we compare them with those computed by other groups. In the case of the orbital solutions, this comparison allows us to determine if they are consistent with those derived using only astrometric data.

6.1 The REB solution

The values of the impact parameters of meteoroid 2014 AA as derived from infrasound data in both the REB and our own determination are based on data from three detecting stations, one located to the north-west in the Northern Hemisphere and two to the south-west across the Equator (see Fig. 1). The hypocentre of the airburst is located in the Northern Hemisphere, but the travel-time model used by the IDC system to derive the origin time is global and has been obtained empirically. It does not account for paths crossing the Equator, where stratospheric winds are typically weaker (Brachet et al. 2010; Green & Bowers 2010; Le Pichon et al. 2012). The REB determination was computed using the global travel-times that are not suited for across the Equator propagation; to compute the origin time, our determination uses the detection time of the closest station to the north-west which is the only one located in the same hemisphere as the hypocentre of the airburst. The origin time in the REB determination is a rather crude estimate of the most probable value.

6.2 Kowalski et al. (2014)

MPEC 2014-A02 (Kowalski et al. 2014) includes a preliminary orbit for 2014 AA: a =1.1660751 AU, e =0.2149211, i =1.°43759, Ω =101.°57475, ω =52.°35440, and M =324.°30925, referred to epoch JD 2456658.5. However, no error estimates are given and that prevents a proper quantitative comparison. Assuming that the uncertainties are similar to those quoted above,[2] this orbital solution seems to be compatible with our findings.

6.3 MPC

The orbital solution available from the MPC[1,12] does not include any error estimates, therefore it is difficult to provide a quantitative assessment of its consistency with our results. It is based on the seven astrometric observations available and it is able to reproduce their values (see Table 6). The root-mean-square deviation with respect to the values in Kowalski et al. (2014) in right ascension amounts to 0.″95, the respective root-mean-square deviation in declination is 0.″30. In principle, it appears to be fully compatible with our findings both geometric and N-body based if the values of the uncertainties are similar to those quoted above.[2]

6.4 NEODyS

The orbital solution available from the Near Earth Objects Dynamic Site[2,13] (NEODyS; Chesley & Milani 1999) is also based on the same seven astrometric observations. Both our geometric and N-body solutions are well within the boundaries of the quoted errors.

6.5 JPL Small-Body Database

Table 1 shows the orbits of 2014 AA as computed by the JPL's Solar System Dynamics group. Using the orbital solution based on both astrometry and infrasound data (second solution in Table 1), the orbital elements of 2014 AA at epoch JD 2456658.628472222 (2014 January 1 03:05:00.0000 TDB) are a = 1.164173034310643 AU, e = 0.2134945866378556, i = 1.°428587405092261, Ω = 101.°6075729620208, ω = 52.°43618813777764, and M = 324.°2172353344642 (source: Horizons On-Line Ephemeris System). These orbital elements and the nominal uncertainties (Δa = 0.010579 AU, Δe = 0.010551, Δi = 0.°073019, $\Delta\Omega$ = 0.°015969, $\Delta\omega$ = 0.°49968, and ΔM = 0.°44168) indicate that our solution is consistent with this determination. If we compare this solution with the one in Table 5, the relative discrepancies in semi-major axis, eccentricity, inclination, longitude of the ascending node, argument of perihelion and time of perihelion passage are: 0.16%, 0.88%, 0.91%, 0.0010%, 0.18%, and 1.1×10^{-6}%. On the other hand, our geometric solution is well within the boundaries of those in Table 1. The comparison with the solution currently displayed by the JPL is given in Sect. 6.7.

6.6 Chesley et al. (2015)

Chesley et al. (2015) applied systematic ranging (Milani & Knežević 2005) to estimate the orbit of 2014 AA. This approach uses the recorded observations as input data. In their table 2 they provide the following solution: a = 1.1694951152059 AU, e = 0.2185819813893022, i = 1.°463031271816491, Ω = 101.°5884374095149, ω = 52.°61778832155812, and τ = 2456704.205054487 JD TDB. This solution is computed

[12] http://www.minorplanetcenter.net/db_search/show_object?object_id=2014+AA

[13] http://newton.dm.unipi.it/neodys

at epoch JD 2456658.8115875920. For this solution the impact happens at 2014 January 2, 02:54:20 (UTC), latitude (°N) = +13.°118, and longitude (°E) = −44.°207. Therefore, its impact time is over 11 minutes earlier than the one obtained from infrasound data and its reported impact latitude is close to the southern edge of the observational solution (see their fig. 5). Chesley et al. (2015) do not provide an indication of the uncertainty and state that their orbit is their best match between orbital and infrasound constraints (see above). For this solution they compute an impact probability of 99.9%.

If we compare this solution with the geometric one in Table 3, left-hand column, we observe the following relative discrepancies in semi-major axis, eccentricity, inclination, longitude of the ascending node, argument of perihelion, and time of perihelion passage: 0.039%, 0.44%, 2.1%, 0.081%, 0.94%, and 0.000017% (using the closest τ). Two completely independent methods produce very similar solutions. This is fully consistent with the results of the quality assessment analysis presented in de la Fuente Marcos & de la Fuente Marcos (2013) and above for the Almahata Sitta event caused by the meteoroid 2008 TC_3.

As for the N-body approach, we have performed an experiment similar to the ones described in Sect. 5 but using the solution in table 2 of Chesley et al. (2015). The following uncertainties have been assumed $\sigma_a = 8.74\times10^{-6}$ AU, $\sigma_e = 5.73\times10^{-6}$, $\sigma_i = 4.^\circ1364\times10^{-5}$, $\sigma_\Omega = 1.^\circ7891\times10^{-6}$, $\sigma_\omega = 7.^\circ6207\times10^{-5}$, and $\sigma_\tau = 1.4155\times10^{-4}$ JD TDB. These values are those of the currently available orbit of 2008 TC_3. Using these conditions, 99.999% of the orbits hit the Earth generating a meteor but nearly 17 minutes (in average) before the impact time in Chesley et al. (2015) and around coordinates latitude (°N) = +13°and longitude (°E) = −44°. The outcome of the experiment is summarized in Fig. 11. If we compare this solution with the one from the N-body approach corrected with astrometry (Table 5), the relative discrepancies in semi-major axis, eccentricity, inclination, longitude of the ascending node, argument of perihelion and time of perihelion passage are: 0.61%, 3.19%, 3.24%, 0.020%, 0.53%, and 3.3×10^{-7}%. Similar differences can be found between this orbital solution and the one in Farnocchia et al. (2016).

6.7 Farnocchia et al. (2016)

Farnocchia et al. (2016) has obtained an improved solution of the pre-impact orbit of 2014 AA. This is the solution currently provided by the JPL Small-Body Database and Horizons On-Line Ephemeris System. Referred to epoch JD 2456658.5, the values of the orbital elements are (see also Table 1):

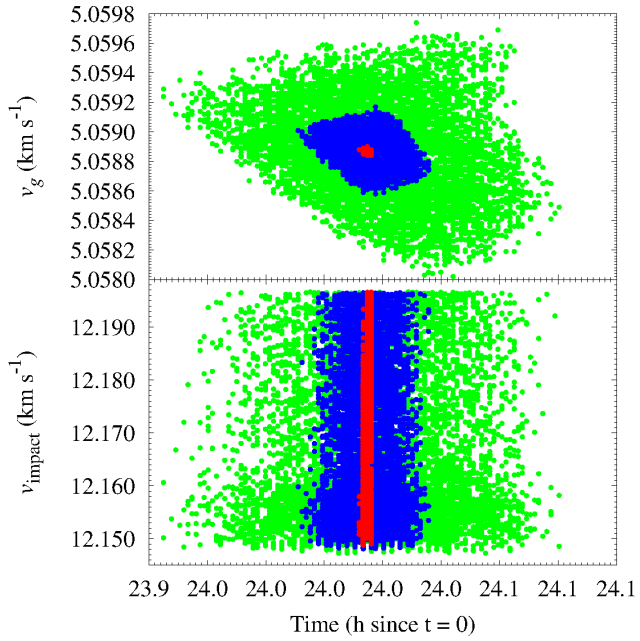

Fig. 10 Values of the v_g and v_{impact} of the virtual impactors as a function of the impact time. Virtual impactor colours as in Fig. 6.

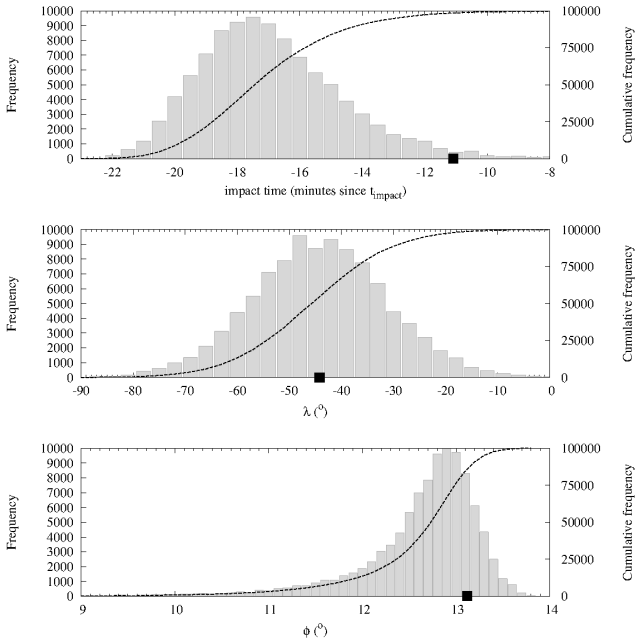

Fig. 11 Resulting distributions in impact parameter space for an experiment analogous to the one in Fig. 3 but using the best match in Chesley et al. (2015) and assumed uncertainties (see the text for details); the values of the best match impact parameters are also indicated (black squares). The impact time is referred to the value based on infrasound data according to Chesley et al. (2015).

a = 1.161570914329746 AU, e = 0.210903385513902, i = 1.°4109467942359, Ω = 101.°613014674528, ω = 52.°3157504212017, and M = 324.°0051879998651. We have downloaded the Cartesian state vector for the epoch JD 2456658.628472222 from the HORIZONS On-Line Ephemeris System and performed a simulation within the same framework used to derive our orbit determination. The values of the geocentric and topocentric coordinates of 2014 AA from this simulation at the times when the original observations of 2014 AA were acquired are shown in Table 7. The root-mean-square deviation with respect to the values in Kowalski et al. (2014) in right ascension amounts to 0.″49, the respective root-mean-square deviation in declination is 0.″31. This integration gives $t_{\rm impact}$ = 2456659.629134 JD TDB, $\lambda_{\rm impact}$= −44.°693, $\phi_{\rm impact}$ = +13.°.070, $h_{\rm impact}$ = 54 km, and $v_{\rm impact}$ = 12.1634 km s^{-1}. The value of the geocentric impact velocity given in Farnocchia et al. (2016) is 12.17 km s^{-1}. On the other hand, the properties of the associated radiant are α_0 = 5.$^{\rm h}$5403, δ_0 = 14.°2723, and $v_{\rm g}$ = 5.05886 km s^{-1}.

In addition, we have computed the evolution of 20,000 control orbits generated using the covariance matrix of this solution as provided by the JPL Small-Body Database (see Sect. 8.2). The results from these simulations are plotted in Figs. 12–15 and can be compared directly with those in Figs. 6–10, red points. It is clear that both solutions are reasonably compatible even if they are based on marginally compatible values of the impact parameters (see Sect. 3). The values of the relative discrepancies in semi-major axis, eccentricity, inclination, longitude of the ascending node, argument of perihelion and time of perihelion passage are: 0.064%, 0.34%, 0.33%, 0.0043%, 0.045%, and 2.8×10^{-7}%. The values of the geocentric and topocentric coordinates of 2014 AA derived from this solution by the JPL at the times when the original observations of 2014 AA were acquired are shown in Table 6. The root-mean-square deviation with respect to the values in Kowalski et al. (2014) in right ascension amounts to 0.″14, the respective root-mean-square deviation in declination is 0.″11. The differences between the root-mean-square deviations as computed by the JPL and the ones from our own calculations (see above) using the same input data are small enough to consider our computational approach as robust.

Table 6 shows that geocentric predictions derived from the MPC and JPL solutions (the current JPL solution is the one in Farnocchia et al. 2016) corresponding to the time frame covered by the observations in Kowalski et al. (2014) are incompatible. There is a systematic offset in declination in the range 17.″8–22.″2 between the geocentric ephemerides derived from these

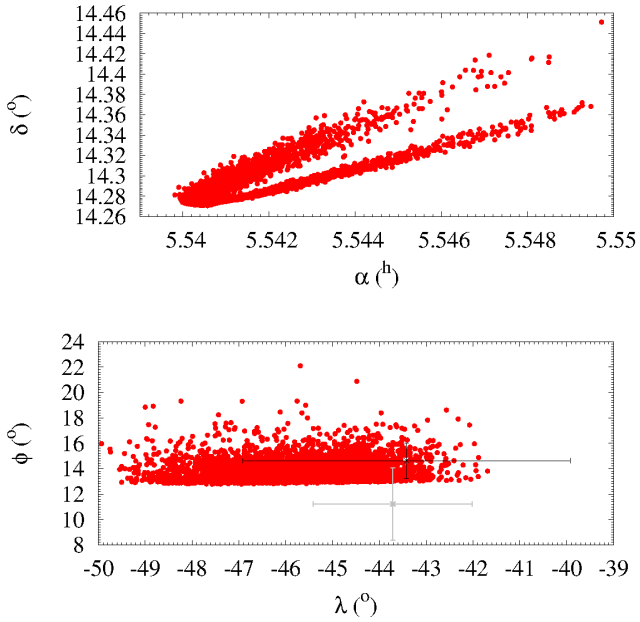

Fig. 12 True radiant geocentric equatorial coordinates (top panel) and their associated virtual impact coordinates (bottom panel) for the solution in Farnocchia et al. (2016); see the text for details. The impact point derived from the infrasound data in Chesley et al. (2015) appears in black with its approximate error bars, our determination presented in Sect. 3 is plotted in grey.

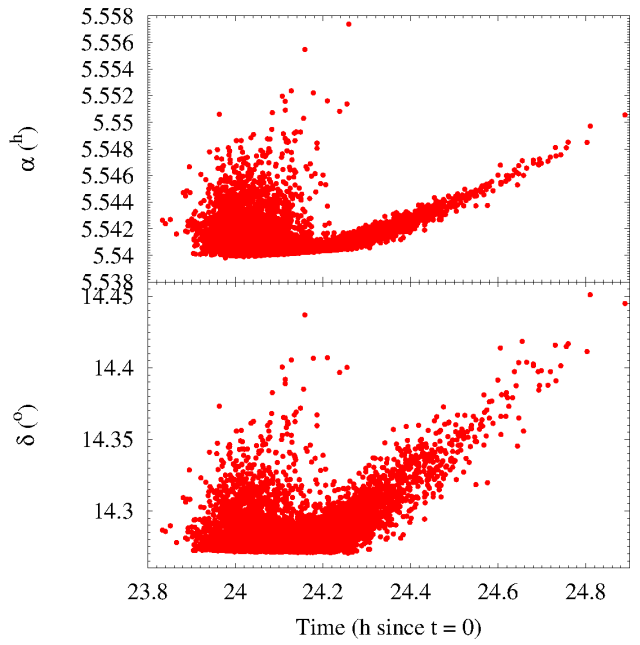

Fig. 13 True radiant geocentric equatorial coordinates of the virtual impactors as a function of the impact time for the solution in Farnocchia et al. (2016).

Table 7 Comparison between the values of the geocentric and topocentric (for observatory code G96, Mt. Lemmon Survey) equatorial coordinates of 2014 AA computed from the solution (integrated by us) in Farnocchia et al. (2016) and the best solution from this work at the times when the observations in Table 6 were acquired (see also Fig. 5). The root-mean-square deviation with respect to the values in Kowalski et al. (2014) in right ascension amounts to 0.″49 for Farnocchia et al. (2016) and to 0.″59 for our solution, the respective root-mean-square deviations in declination are 0.″31 and 0.″28.

Source	Farnocchia et al. (2016)				This work			
	topocentric		geocentric		topocentric		geocentric	
DATE UTC	R.A. (J2000)	Decl.	R.A. (J2000)	Decl.	R.A. (J2000)	Decl.	R.A. (J2000)	Decl.
2014 01 01.26257	05:32:35.55	+13:59:44.6	05:32:39.35	+14:16:14.1	05:32:35.51	+13:59:44.6	05:32:39.31	+14:16:14.2
2014 01 01.26896	05:32:28.87	+13:59:36.3	05:32:40.21	+14:16:13.8	05:32:28.82	+13:59:36.3	05:32:40.17	+14:16:13.9
2014 01 01.28176	05:32:15.27	+13:59:16.0	05:32:41.96	+14:16:13.2	05:32:15.22	+13:59:16.0	05:32:41.91	+14:16:13.2
2014 01 01.30701	05:31:47.96	+13:58:21.3	05:32:45.57	+14:16:11.9	05:31:47.90	+13:58:21.2	05:32:45.51	+14:16:11.9
2014 01 01.30828	05:31:46.58	+13:58:18.0	05:32:45.76	+14:16:11.8	05:31:46.52	+13:58:17.9	05:32:45.70	+14:16:11.8
2014 01 01.30955	05:31:45.20	+13:58:14.7	05:32:45.94	+14:16:11.8	05:31:45.13	+13:58:14.6	05:32:45.88	+14:16:11.7
2014 01 01.31081	05:31:43.83	+13:58:11.3	05:32:46.13	+14:16:11.7	05:31:43.76	+13:58:11.2	05:32:46.07	+14:16:11.7

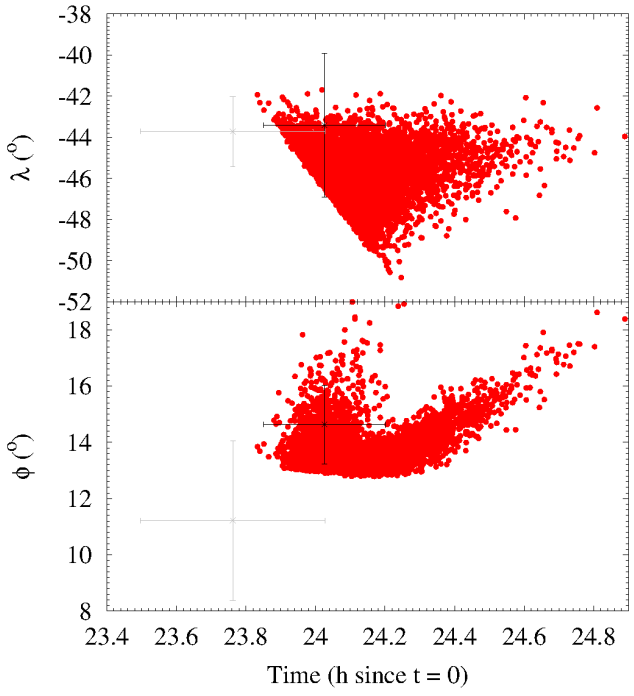

Fig. 14 Impact coordinates of the virtual impacts as a function of the impact time for the solution in Farnocchia et al. (2016). The impact point derived from the infrasound data in Chesley et al. (2015) appears in black with error bars, our determination presented in Sect. 3 is plotted in grey.

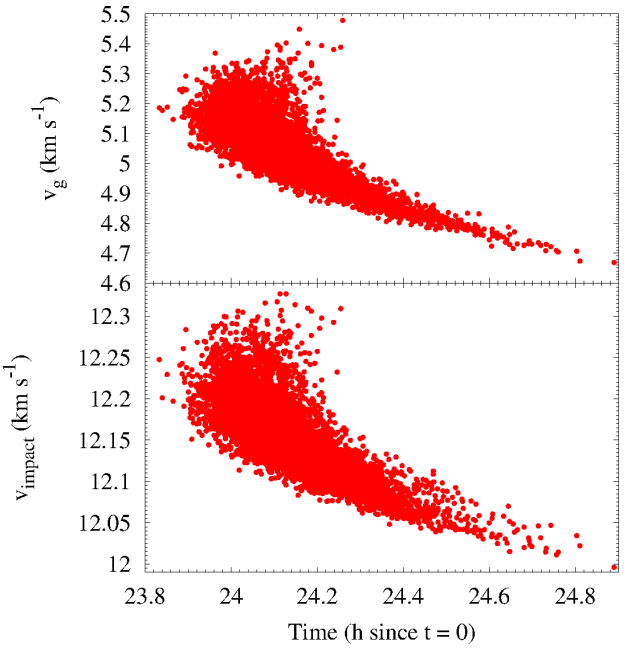

Fig. 15 Values of the $v_{\rm g}$ and $v_{\rm impact}$ of the virtual impactors as a function of the impact time for the solution in Farnocchia et al. (2016).

solutions in that time frame. There are also significant differences in right ascension but always $<17\farcs8$. However, the topocentric predictions are both nearly perfect matches of the observational data in Kowalski et al. (2014). Table 7 shows the coordinate predictions from the nominal orbits in Farnocchia et al. (2016) and our own, integrated and processed under the same conditions (see also Fig. 5). We observe that the geocentric values from the JPL solution (computed by the JPL) in Table 6 and those of Farnocchia et al. (2016) in Table 7 are nearly perfect matches (differences below $0\farcs2$); consistently, similar deviations are observed for the topocentric values. The slight discrepancies may be the result of using different formulae for the various conversions. In any case, these very small differences should have no effects on the study of both the past dynamical evolution of 2014 AA and the possible existence of other objects moving in similar orbits among the known NEOs.

7 Peeking into the past of 2014 AA

We have used the solution displayed in Table 5 and the same N-body techniques described above to further investigate the past dynamics of 2014 AA. Figure 16 shows that this object has remained in the orbital neighbourhood of our planet for several thousands of years. It was only relatively recently (∼2.5 kyr ago) that it started to undergo close encounters with Mars at aphelion (descending node), although the nodes (e.g. ascending) had been close to Mars in the past (see panel G, Fig. 16). The object experienced very close encounters with the Earth–Moon system in the past and that explains its highly chaotic orbital evolution (see panels A and C, Fig. 16).

However, the most striking feature in Fig. 16 appears in the time evolution of ω (panel F). This orbital parameter does not circulate smoothly (i.e., take any possible value) as in the case of a passing body and it librated around 180°from about 40 to 14 kyr ago, then again from 9 kyr to 2 kyr. The object was starting a libration about $\omega \sim 0°$ when the impact took place. These are the signposts of one of the variants of the Kozai resonance (Kozai 1962). An argument of perihelion librating around 180°implies that the associated object reaches perihelion at approximately the same time it crosses the Ecliptic from North to South (the descending node). Perihelion at the ascending node is linked to $\omega \sim 0°$; meteoroid 2014 AA found our planet at the ascending node. When the Kozai resonance occurs at low inclinations, the argument of perihelion librates around 0°or 180°(see e.g. Milani et al. 1989).

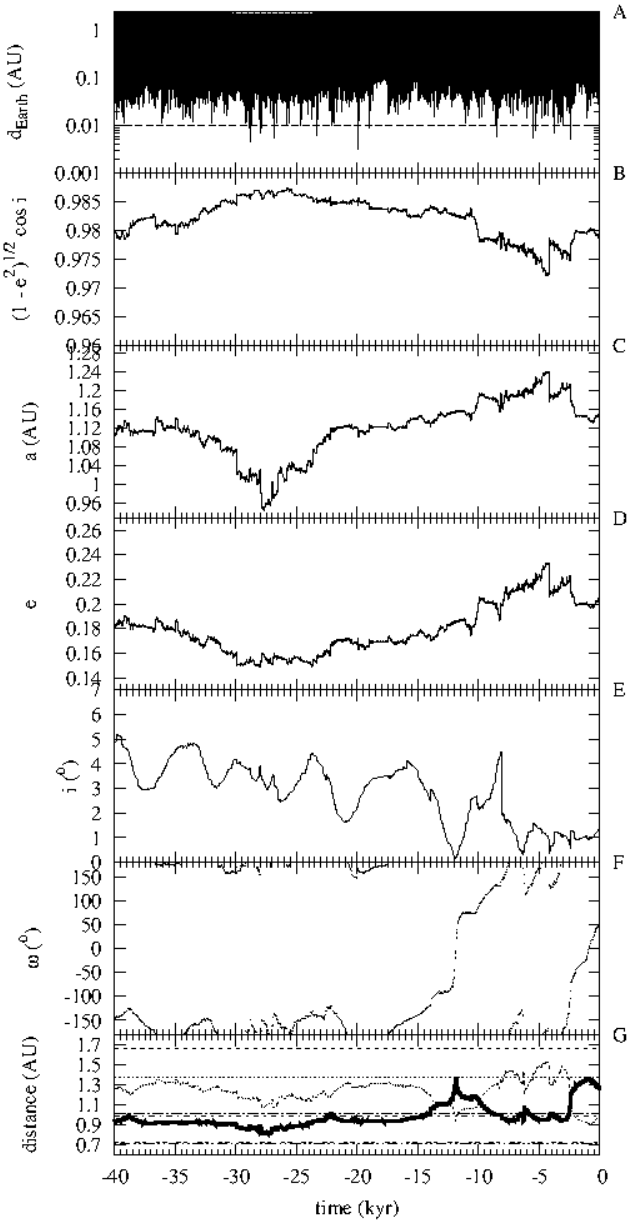

Fig. 16 Time evolution of various parameters for the orbital solution of 2014 AA in Table 5. The distance from the Earth (panel A); the value of the Hill sphere radius of the Earth, 0.0098 AU, is displayed. The parameter $\sqrt{1-e^2}\cos i$ (panel B). The orbital elements a (panel C), e (panel D), i (panel E) and ω (panel F). The distance to the descending (thick line) and ascending nodes (dotted line) is in panel G. Planetary perihelion and aphelion distances (Venus, Earth, and Mars) are also shown.

Michel & Thomas (1996) confirmed that, at low inclinations, the argument of perihelion of some NEOs can librate around either 0°or 180°. This topic received additional attention from Namouni (1999).

The Kozai-controlled past evolution of this object is firmly established, we have integrated 50 control orbits derived from the orbital solution in Table 5, assuming a normal distribution in orbital parameter space, and all of them exhibit this behaviour during the last 15 kyr or so. The only difference is in the timing of the episodes, when it switches from libration around 180°to other states. Some control orbits, in the dynamical neighbourhood of the one plotted, exhibit libration of the argument of perihelion around 180°for most of the time interval displayed in Fig. 16. The evolution of the value of the distance from the nodes to the Sun (panel G in Fig. 16) is clearly coupled with the behaviour of ω. The values of eccentricity and inclination are also coupled when ω librates ($\sqrt{1-e^2}\cos i \approx$ constant, see panel B in Fig. 16) although the oscillation in e is difficult to observe due to superposition of secular resonances (see below).

The overall evolution of 2014 AA in Fig. 16 appears to be rather chaotic, perhaps secularly chaotic. This secular evolution is best studied in the $e_{\rm r}\omega_{\rm r}$-plane, where $e_{\rm r} = e - e_{\rm p}$ and $\omega_{\rm r} = \omega - \omega_{\rm p}$, $e_{\rm p}$ and $\omega_{\rm p}$ are, respectively, the eccentricity and argument of perihelion of a given planet (Namouni 1999). Our $e_{\rm r}\omega_{\rm r}$ maps look very irregular (see Fig. 17) and 2014 AA suffers secular interactions that induce librations of its relative argument of perihelion with respect to our planet but also to Venus, Mars, and Jupiter. The topic of overlapping secular resonances and its effects on the dynamics of asteroids was first studied by Michel (1997) in the particular case of objects moving in Venus horseshoe orbits. He concluded that overlapping of secular resonances is possible, complicating the dynamics of horseshoe orbits significantly. Asteoroid 2014 AA does not appear to have experienced co-orbital (horseshoe or any other type) episodes with our planet in the immediate past. Figure 17 shows that the secular behaviour of this object with respect to Venus and the Earth was rather similar, with oscillation of their respective $\omega_{\rm r}$ around 180°until about 13 kyr before impact. For Mars, the coupling is also obvious during the same period of time, although its $\omega_{\rm r}$ librates about 90°for most of the displayed time and around $-90°$ as the impact time approaches. As for Jupiter, it librated around $-90°$ for most of the displayed time. The actual source of the observed secular behaviour is Jupiter. If Jupiter is not included in the calculations, the secular chaos vanishes.

The calculations in Namouni (1999) were made within the context of the restricted elliptic three-body

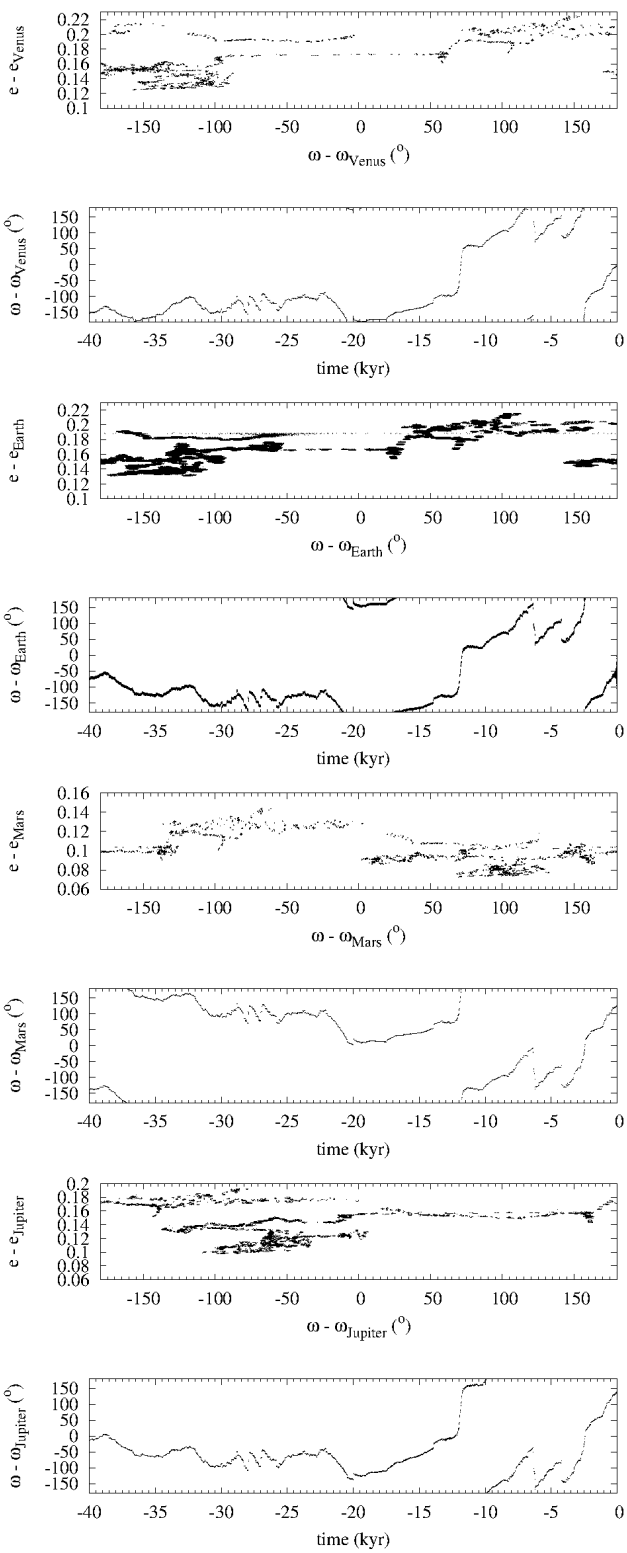

Fig. 17 The $e_{\rm r}\omega_{\rm r}$-portrait for the orbital solution of 2014 AA relative to Venus, the Earth, Mars, and Jupiter. Data as in Fig. 16.

problem. The dynamical situation here is significantly more complicated. An external perturber, that is not interacting directly with 2014 AA, induces the secular behaviour observed and the entire system of overlapping secular resonances drives the evolution of the meteoroid. If Jupiter is removed, the librations of the relative argument of perihelion of 2014 AA with respect to the other planets cease immediately. This behaviour is expected as the terrestrial planets share the effect of the secular perturbation from Jupiter (see e.g. Ito & Tanikawa 1999, 2002; Tanikawa & Ito 2007). The reported secular behaviour is quite consistent across control orbits. This web of overlapping secular resonances appears to keep the semi-major axis of this object confined within the neighbourhood of the Earth for extended periods of time. This may also have played a role in facilitating the eventual impact. Given its marginal stability (the value of the semi-major axis remains fairly stable during some of the displayed evolution), this subdomain of the NEO orbital parameter realm may host additional objects and this interesting possibility is explored in the following section.

8 Possible related objects and their stability

It has been argued that some of the recent, most powerful Earth impacts may be associated with resonant groups of NEOs and/or very young meteoroid streams (de la Fuente Marcos & de la Fuente Marcos 2015a). Both 2008 TC_3 and 2014 AA caused atmospheric impact events or airbursts that released an amount of energy equivalent to about one kiloton of Trinitrotoluene (TNT) explosives (Jenniskens et al. 2009; Chesley et al. 2015); therefore, they can be included among the low-yield members of the group of recent, most powerful Earth impacts with the Chelyabinsk Event occupying the top of the scale (Brown et al. 2013). Since 2000, the CTBTO infrasound sensors of the IMS network (Le Pichon et al. 2012) have detected at least 26 events related to asteroid impacts with an individual energy in excess of 1 (and up to ∼500) kt of TNT equivalent.[14] The most extraordinary event recorded so far by the IMS network is the Chelyabinsk superbolide, on 2013 February 15 (Brown et al. 2013; Le Pichon et al. 2013; Pilger et al. 2015).

8.1 Dynamically-related objects?

Assuming that 2014 AA may have been a fragment of a larger body and/or that other objects could be moving in similar orbits if they are trapped in some web of secular resonances like the one described in the previous section, here we try to single out candidates to be following somewhat similar orbits. The dynamical evolution of these potentially similar minor bodies is further studied to confirm or reject a putative dynamical link between 2014 AA and the selected candidates.

In order to identify suitable candidates we use the D-criteria of Southworth & Hawkins (1963), $D_{\rm SH}$, Lindblad & Southworth (1971), $D_{\rm LS}$ (in the simplified form of eqn. 1 in Lindblad 1994 or eqn. 1 in Foglia & Masi 2004), Drummond (1981), $D_{\rm D}$, and the $D_{\rm R}$ from Valsecchi et al. (1999). A search among NEOs currently catalogued (as of 2016 July 31) by the JPL Small-Body Database[15] using these criteria gives the list in Table 8. The objects are sorted by ascending $D_{\rm LS}$. Only objects with $D_{\rm LS}$ and $D_{\rm R} < 0.05$ are shown, which is a somewhat arbitrary but conservative choice within the NEO context (see e.g. de la Fuente Marcos & de la Fuente Marcos 2016). The D-criteria have been computed with respect to the solution displayed in Table 5. We must emphasize that the use of the various D-criteria is a helpful device to single out candidates suitable for further study; we are not assuming that a low value of one or more of the D-criteria computed using osculating orbital elements must necessarily imply any physical or dynamical link between two given objects.

[14] http://newsroom.ctbto.org/2014/04/24/ctbto-detected-26-major-asteroid-impacts-in-earths-atmosphere-since-2000/

[15] http://ssd.jpl.nasa.gov/sbdb.cgi

Table 8 Orbital elements, orbital periods ($P_{\rm orb}$), perihelia ($q = a\ (1-e)$), aphelia ($Q = a\ (1+e)$), number of observations (n), data-arc, absolute magnitudes (H) and MOID of minor bodies with orbits similar to that of the meteoroid 2014 AA (as in Table 5). The various D-criteria ($D_{\rm SH}$, $D_{\rm LS}$, $D_{\rm D}$ and $D_{\rm R}$) are also shown. The objects are sorted by ascending $D_{\rm LS}$ (eqn. 1 in Lindblad 1994). Only objects with $D_{\rm LS}$ and $D_{\rm R} < 0.05$ are shown. The orbit of 2014 AA is the solution displayed in Table 5 that is referred to the epoch JD 2456658.628472222. The orbits of the other objects are referred to the Epoch 2457600.5 (2016-July-31.0) TDB (Barycentric Dynamical Time) with the exceptions of 2009 SH_1 that is referred to 2455092.5 (2009-September-18.0) and 2015 MZ_{53} that is referred to 2457194.5 (2015-June-21.0). Data as of 2016 July 31.

Asteroid	a (AU)	e	i (°)	Ω (°)	ω (°)	$P_{\rm orb}$ (yr)	q (AU)	Q (AU)	n	arc (d)	H (mag)	MOID (AU)	$D_{\rm SH}$	$D_{\rm LS}$	$D_{\rm D}$	$D_{\rm R}$
2014 AA	**1.16231**	**0.21161**	**1.41559**	**101.60863**	**52.33925**	**1.26**	**0.91635**	**1.40827**	–	–	**30.90**	**0.0000005**	–	–	–	–
2011 JV_{10}	1.13988	0.20225	1.40510	221.37001	297.53422	1.22	0.90934	1.37043	18	2	29.70	0.00130	0.04762	0.01170	0.02739	0.04182
2011 GJ_3	1.14129	0.20439	0.84382	331.06066	308.53533	1.22	0.90801	1.37456	38	20	26.20	0.00357	0.37201	0.01487	0.14677	0.04106
2012 DJ_{54}	1.17610	0.22986	1.99084	336.88562	120.04517	1.28	0.90577	1.44644	25	17	28.60	0.00163	0.21820	0.02336	0.08311	0.02792
2015 MZ_{53}	1.14419	0.18837	2.20730	259.66059	298.31300	1.22	0.92865	1.35972	7	2	27.50	0.00054	0.16437	0.02971	0.07886	0.02157
2007 HC	1.15510	0.20717	3.15638	216.84639	57.97253	1.24	0.91580	1.39440	31	6	25.20	0.00331	0.37076	0.03071	0.14257	0.02658
2012 UY_{68}	1.17489	0.22823	2.90143	70.31433	35.75187	1.27	0.90675	1.44303	46	24	25.00	0.01743	0.18231	0.03226	0.07059	0.03450
2013 RV_9	1.16511	0.19902	3.50067	332.82949	108.32269	1.26	0.93323	1.39699	88	183	23.60	0.02268	0.25691	0.04204	0.09239	0.02910
2013 UM_9	1.21328	0.24618	2.93258	38.92410	283.29746	1.34	0.91459	1.51197	32	13	24.80	0.01826	0.45899	0.04358	0.22727	0.03576
2013 HO_{11}	1.19448	0.23414	3.71878	59.05671	245.90995	1.31	0.91481	1.47416	81	251	23.00	0.00564	0.43503	0.04611	0.19423	0.02404
2009 SH_1	1.19832	0.24599	3.32567	354.92542	294.87464	1.31	0.90355	1.49310	11	1	29.40	0.00399	0.43131	0.04957	0.18978	0.04105
2004 XK_3	1.22784	0.26053	1.48182	57.91377	304.67526	1.36	0.90795	1.54772	240	1464	24.40	0.00095	0.46053	0.04964	0.22403	0.04411

Apollo asteroids 2011 GJ_3 (McMillan et al. 2011), 2011 JV_{10} (Kowalski et al. 2011), and 2012 DJ_{54} (Micheli et al. 2012) follow very similar orbits at present. The relative D_{SH}, D_{LS}, D_D, and D_R of 2011 GJ_3 and 2011 JV_{10} are 0.35488, 0.01011, 0.13679, and 0.00119, respectively. In the case of 2011 GJ_3 and 2012 DJ_{54} the values are 0.435352, 0.0324687, 0.221674, and 0.0286270. Their orbits are rather uncertain but they might be related, with 2011 JV_{10} and 2012 DJ_{54} perhaps being relatively recent fragments of 2011 GJ_3. But having similar orbits at present time is not enough to claim a relationship, dynamical or otherwise; a representative set of orbits must be integrated to show that the dynamical evolution over a reasonable amount of time is also similar (see e.g. Porubcan et al. 2006; Jopek & Williams 2013).

Figure 18 shows the short-term evolution of the orbital elements a, e, i, Ω, and ω of 2011 GJ_3, 2011 JV_{10}, 2012 DJ_{54}, 2013 NJ_4, and 2014 AA. The left-hand panels show the average evolution of 100 control orbits (see Sect. 8.2 for additional details), the right-hand panels show the ranges in the values of the parameters at the given time. The orbits of 2014 AA and 2011 GJ_3 are alike, their past orbital evolution also being quite similar (see Fig. 18). Not included in Table 8 —because it does not comply with the restriction D_{LS} and $D_R < 0.05$ with respect to 2014 AA— is meteoroid 2013 NJ_4 (Wainscoat et al. 2013; a = 1.13324 AU, $e = 0.20253$, $i = 1\overset{\circ}{.}31952$, $\Omega = 115\overset{\circ}{.}60660$, $\omega = 238\overset{\circ}{.}50930$, $H = 27.40$ mag, MOID = 0.0046 AU) that also has low relative D_{SH}, D_{LS}, D_D and D_R with respect to 2011 GJ_3: 0.24901, 0.00953, 0.08515, and 0.02152. Given the uncertainty of their current orbital solutions it cannot be discarded that 2011 GJ_3, 2011 JV_{10}, 2012 DJ_{54}, 2013 NJ_4, and 2014 AA (see Table 9) are the result of an asteroid break-up that took place perhaps 1,800 to 1,400 yr ago (see Fig. 18).

Figure 19 shows the average time evolution of the various D-criteria for 2011 GJ_3, 2011 JV_{10}, 2012 DJ_{54}, and 2013 NJ_4 with respect to 2014 AA as described by the data in Fig. 18, left-hand panels. This type of analysis is customarily used to link meteors and NEOs (see e.g. Trigo-Rodríguez et al. 2007; Olech et al. 2015). From the figures, a catastrophic disruption event around 1,600 yr ago cannot be ruled out. In terms of statistics, these objects are probable dynamical relatives: the ranges of their orbital parameters, a, e, and i, fully overlap after less than 100 yr of backwards integration. Schunová et al. (2012) have shown that a robust statistical estimate of a dynamical relationship between objects part of the near-Earth asteroid (NEA) population is only possible for groups of four and more objects although they could not find any statistically significant group of dynamically related objects among those known at that time. All the objects in the candidate group of dynamically related asteroids proposed here were discovered after the completion of the analysis in Schunová et al. (2012) that considered 7,563 NEOs (through 2011 DW). According to that analysis, this group of objects may be an asteroid cluster and perhaps have a common origin as the values of their D_{SH} are < 0.060 for most or all of them nearly 1,600 yr ago. Although the available orbital solutions for these objects are rather poor (see Table 9), the evidence provided by Figs. 18 and 19 in favour of a common origin is certainly encouraging (but still far from conclusive). In any case, it must be emphasized that false asteroid clusters may be identified as a result of significant orbital element uncertainties (Schunová et al. 2012). Here, we have tried to reduce this effect by using the average time evolution of the various D-criteria (see Fig. 19).

Asteroid 2011 JV_{10} reached perigee on 2011 May 5 at a geocentric distance of 0.0023 AU. In spite of its small size ($H = 29.7$ mag or ∼7 m) it attracted considerable attention because it became an obvious example of the Red Baron dynamical scenario (Adamo 2011) in which a small body approaches the Earth from out of the Sun's glare, as the parent body of the Chelyabinsk superbolide did (Popova et al. 2013). Red Baron scenario events are rather frequent and objects moving in 2011 JV_{10}-like orbits appear to be prone to them. In addition to their Kozai-like dynamics (compare Figs. 16 and 20), this group of objects share a number of peculiar dynamical features. They reach perigee within one or two months of reaching perihelion. Earth approaches can occur before or after perihelion. When they occur after perihelion, these objects approach the Earth from its day side. In this configuration, the incoming object cannot be discovered until after perigee as it was the case of 2011 JV_{10}. Even if they approach from the night side, when the encounter takes place at the ascending node (as in the case of 2014 AA) the object will move south from the Ecliptic. That area of the sky receives less attention than the northern one because there are less telescopes (and less land masses) south from the equator. After the encounter, they become part of the day-time sky and, therefore, no longer observable from the ground. This suggests that these objects are relatively difficult to detect if they are all as small as 2011 GJ_3 (17–38 m) or smaller; their windows of optimal visibility would be too short —perhaps no more than a few days. This is consistent with the fact that most of them have very short arcs, eight of them have arcs shorter than a month. Asteroid 2011 GJ_3 may have a size similar to that of the Chelyabinsk impactor.

Among the objects included in Table 8, the largest is 2013 HO_{11} (Ries et al. 2013) with an absolute magni-

Table 9 Heliocentric Keplerian orbital elements of 2011 JV_{10}, 2011 GJ_3, 2012 DJ_{54}, and 2013 NJ_4 used in this research. Values include the 1σ uncertainty. The orbits are computed at epoch JD 2457600.5 that corresponds to 0:00 TDB on 2016 July 31 (J2000.0 ecliptic and equinox). Source: JPL Small-Body Database.

		2011 JV_{10}	2011 GJ_3	2012 DJ_{54}	2013 NJ_4
Semi-major axis, a (AU)	=	1.1399±0.0002	1.1413±0.0003	1.1761±0.0002	1.13324±0.00007
Eccentricity, e	=	0.2023±0.0002	0.2044±0.0003	0.2299±0.0002	0.20253±0.00008
Inclination, i (°)	=	1.4051±0.0012	0.8438±0.0015	1.9908±0.0014	1.3195±0.0004
Longitude of the ascending node, Ω (°)	=	221.370±0.002	331.06±0.03	336.8856±0.0002	115.6066±0.0007
Argument of perihelion, ω (°)	=	297.534±0.004	308.54±0.02	120.0452±0.0003	238.5093±0.0007
Mean anomaly, M (°)	=	155.4±0.3	69.1±0.6	208.6±0.3	145.81±0.08
Perihelion, q (AU)	=	0.90934±0.00007	0.90801±0.00015	0.90577±0.00005	0.90373±0.00004
Aphelion, Q (AU)	=	1.3704±0.0002	1.3746±0.0004	1.4464±0.0002	1.36275±0.00008
Absolute magnitude, H (mag)	=	29.7	26.2	28.6	27.4

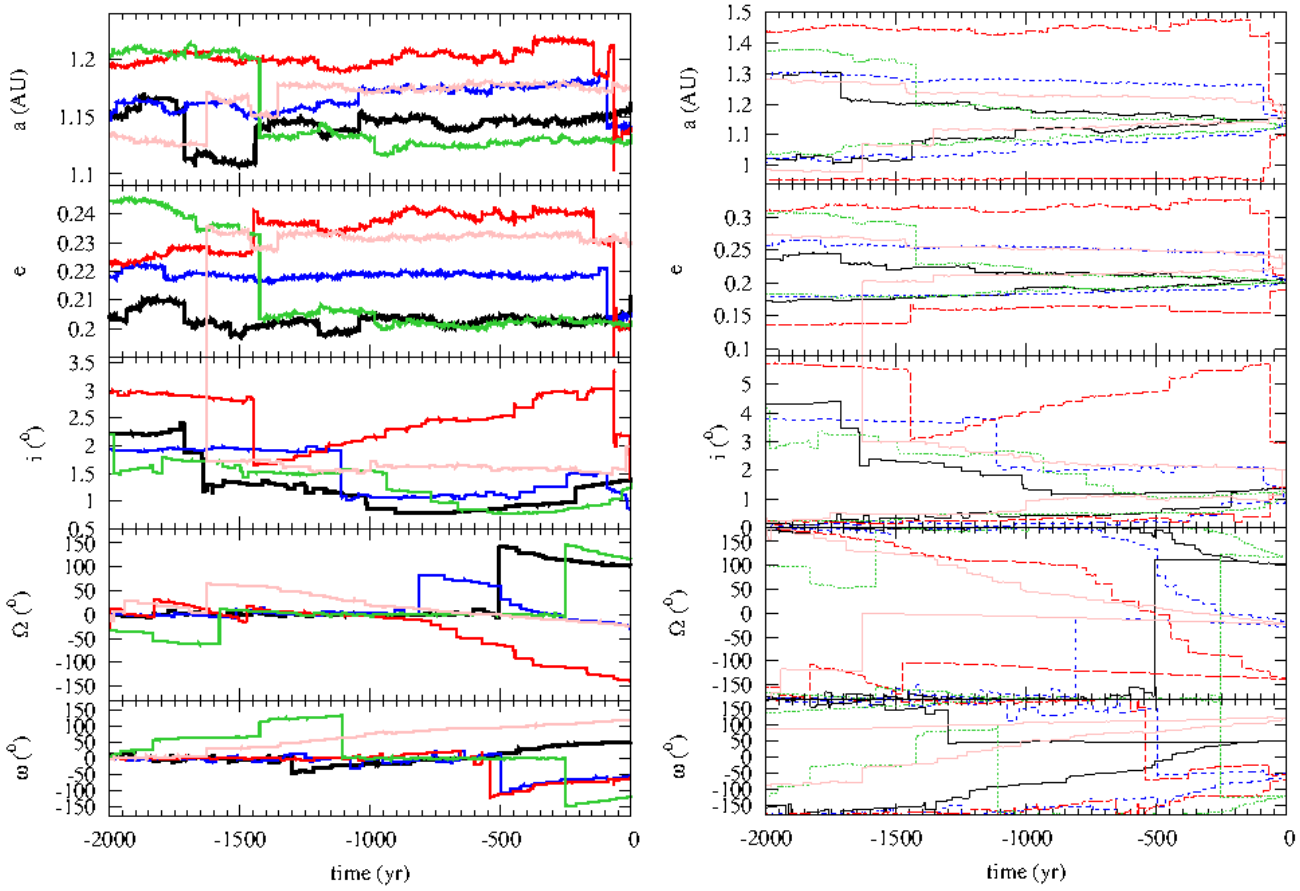

Fig. 18 Time evolution of the orbital elements a, e, i, Ω, and ω of 2011 JV_{10} (red line), 2011 GJ_3 (blue line), 2012 DJ_{54} (pink line), 2013 NJ_4 (green line), and 2014 AA (black line) as described by the solution displayed in Table 5. The left-hand panels show the average evolution of 100 control orbits, the right-hand panels show the ranges in the values of the parameters at the given time.

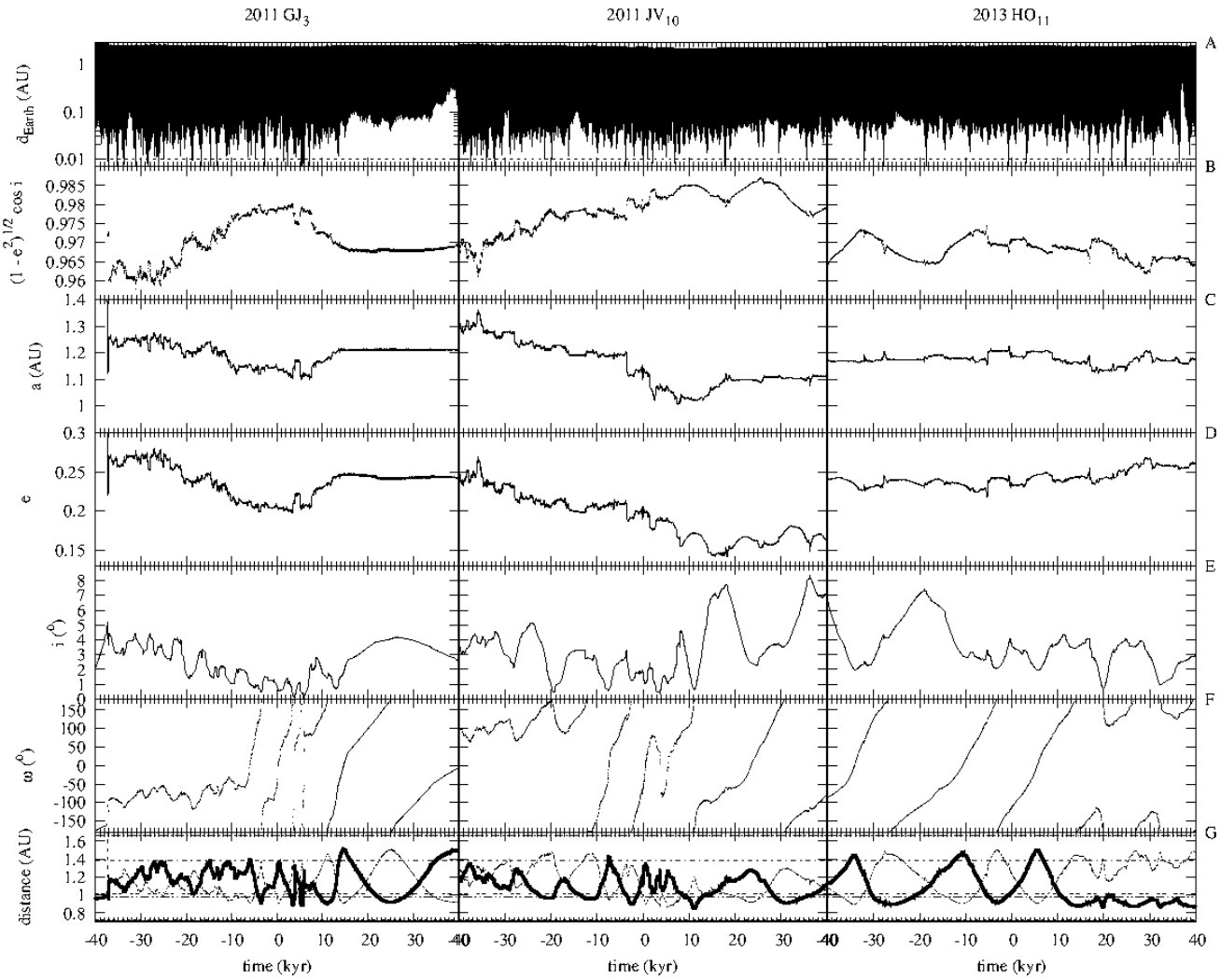

Fig. 20 Time evolution of various parameters for the nominal orbital solutions of 2011 GJ_3, 2011 JV_{10}, and 2013 HO_{11}. The distance from the Earth (panel A); the value of the Hill sphere radius of the Earth, 0.0098 AU, is displayed. The parameter $\sqrt{1-e^2}\cos i$ (panel B). The orbital elements a (panel C), e (panel D), i (panel E) and ω (panel F). The distance to the descending (thick line) and ascending nodes (dotted line) is in panel G. Planetary perihelion and aphelion distances (Earth and Mars) are also shown. These integrations are referred to the JD 2456600.5 epoch.

tude of 23.0 (diameter 75–169 m) and a MOID of 0.006 AU. Its orbit is also one of the most statistically robust. Figure 20 shows the orbital evolution of 2011 GJ_3, 2011 JV_{10}, and 2013 HO_{11}. As 2014 AA did, the three objects may remain within the immediate neighbourhood of our planet for dozens of thousands of years. Asteroids 2011 GJ_3 and 2011 JV_{10} exhibit Kozai-like dynamics; 2013 HO_{11} will experience this behaviour in the future but now its argument of perihelion circulates. This object is currently outside the web of overlapping secular resonances pointed out above. From a strictly dynamical standpoint, 2013 HO_{11} and most of the objects in Table 8 are not like the five objects 2011 GJ_3, 2011 JV_{10}, 2012 DJ_{54}, 2013 NJ_4, or 2014 AA; they are not subjected to Kozai resonances now but they may have been Kozai resonators in the past or become ones in the future. Taking into account that the orbits of the five objects are poorly constrained (perhaps with the exception of 2014 AA), it is not possible to confirm a putative common origin for these objects, but it cannot be ruled out either.

At this point one may argue that, within a large sample of minor bodies, it is always possible to identify groups of a few objects with values of the various D-criteria as low as the threshold used here and this has no real dynamical implications. Therefore, what is the statistical significance of our findings, if any? In other words, given an orbital solution like the one displayed in Table 5, how high is the theoretical likelihood of finding one or more objects with $D_{\rm LS}$ and $D_{\rm R} < 0.05$? The NEOSSat-1.0 orbital model (Greenstreet et al. 2012) is widely regarded as one of the best models available to describe the orbital distribution of the NEO population. Synthetic data from this model do not contain any physically related objects, but they may include dynamically related virtual objects as the model is the result of extensive numerical integrations. Within the synthetic data, groups of objects following similar dynamical pathways could still be found because the integrations can reproduce the web of overlapping resonances that permeates the region. In order to check the statistical significance of our findings, we have used the codes described in Greenstreet et al. (2012)[16] with the same standard input parameters to generate sets of orbital elements of about 15,000 virtual objects (the NEOs currently known amount to 14,759 objects). These datasets have been processed using the same algorithm applied above to real data in order to single out the objects in Table 8.

Let us assume that the size and orbital elements of asteroids are uncorrelated. Ignoring the values of the absolute magnitude (NEOSSat-1.0 was originally developed for NEOs with $H < 18$ mag) and only performing the processing in terms of orbits, the search produced no results. We had to double the value of the threshold to obtain an average of one virtual object. Although not fully conclusive, this experiment suggests that our findings may be somewhat robust and that objects in this group could be truly (dynamically and/or genetically) related. However, genetically related asteroids can only be confirmed spectroscopically and none of these objects have been observed spectroscopically yet. In this context, it is rather surprising that if we apply the same approach to 2008 TC_3 a few compatible virtual objects can be readily found. Table 8 includes 11 objects with $D_{\rm LS}$ and $D_{\rm R} < 0.05$ with respect to the orbital solution in Table 5; a similar analysis for 2008 TC_3 using real data produces 24 candidates. However, using larger synthetic datasets, the results suggest that objects moving in 2008 TC_3-like orbits are nearly three times more likely to exist than those following 2014 AA-like orbits. Not accounting for observational biases, this may be tentatively interpreted as pointing to an intrinsically different origin for 2008 TC_3 and 2014 AA.

Schunová et al. (2014) have studied the expected dynamical signature of a catastrophic asteroidal disruption during a very close Earth approach. These authors have found that the minimum size of a progenitor capable of producing an observable NEO family (a group of objects genetically, not just dynamically, related) is about 350 m in diameter. Such asteroid family would be observable for about 2000 yr and include a few million fragments with sizes in the 1–10 m range. Schunová et al. (2014) have also found that formation of tidally-disrupted NEO families is enhanced for objects following orbits with 0.5 AU $< a <$ 1.25 AU, $e <$0.5, and $i <$5°which is the case of the group of minor bodies discussed here. If the objects moving in 2014 AA-like orbits are physically related, i.e. they are the result of a catastrophic disruption event, many more should be detected over the next few decades. They could be intrinsically difficult to detect though (see above). However, if this group of objects is just a resonant family (or even a random grouping) without a common physical origin, the number of objects moving in such orbits could be relatively small. Genetic asteroid families have been known for about a century (see e.g. Hirayama 1918; Zappalà et al 1990, 1994); dynamical asteroid families or dynamical groups are asteroids temporarily trapped in a mean motion or secular resonance (or a web of overlapping ones). Genetic families may exist within dynamical groups, like in the case of the Hildas (Brož & Vokrouhlický 2008).

It may be argued that any conclusions drawn from a set of orbital solutions based on few observations and

[16] http://www.phas.ubc.ca/∼sarahg/n1model/

short arcs are nothing but mere speculation. However, we are dealing here with objects that are very small and because of this can only be discovered and recovered when they pass very close to our planet. Their observational windows are therefore exceptionally short and in some cases well spaced due to the influence of secular resonances (Kozai-like behaviour). If the existence of objects moving in similar orbits is systematically neglected based on their relatively poor orbital solutions, their orbits are not going to be improved in the future simply because they are not going to attract any attention. In the present case, we have a meteoroid that actually hit the Earth and a few comparably small bodies that move in rather similar orbits with small MOIDs. Asteroid 2012 DJ_{54} is included in the list of potential future Earth impact events compiled by the JPL Sentry System with an impact probability of 2.0×10^{-4};[17] asteroid 2009 SH_1 is also included with an impact probability of 7.0×10^{-8}.[18] These facts clearly deserve further attention as the data may hint at a relatively recent asteroid break-up. In addition, the past orbital evolution of these objects strongly suggest that they have remained in the neighbourhood of the Earth–Moon system and away from the main asteroid belt for many thousands of years. If the objects have a common origin, the fragmentation episode that created them may have happened relatively recently in astronomical terms (see Fig. 18). This means that catastrophic disruption events, perhaps due to rotational disruptions (Denneau et al. 2015), may not only be taking place in the main belt but also among the closest NEOs. The possible production of meteoroids within the immediate neighbourhood of our planet has an obvious and direct effect on the evaluation of the overall asteroid impact hazard (e.g. Schunová et al. 2014). Fortunately, although this is of considerable theoretical interest, most of these fragments are small enough to be of less concern in practice.

It may also be argued that ignoring the Yarkovsky and YORP effects for these objects may seriously hamper our qualitative understanding of their dynamics; however, the integrations completed here hint at semimajor axis drifts < 0.3 AU over time-scales of dozens of kyr. The largest predicted Yarkovsky drift rates are $\sim10^{-7}$ AU yr^{-1} (see e.g. Farnocchia et al. 2013); a simple estimate shows that, in order to produce a semimajor axis drift comparable to those observed in Figs. 16 or 20 at the largest Yarkovsky drift rate, several Myr are required. The uncertainties in the orbital parameters of these objects grow only moderately after 1 kyr or so (see Fig. 18, right-hand panels), therefore the previous discussion on their long-term orbital evolution as well as the comparisons made above are likely valid.

[17] http://neo.jpl.nasa.gov/risk/2012dj54.html

[18] http://neo.jpl.nasa.gov/risk/2009sh1.html

8.2 Average short-term orbital evolution: MCCM

Figure 18 shows the short-term evolution of the orbital elements a, e, i, Ω, and ω of the objects studied here, including the probable orbit of 2014 AA in Table 5. In the figures, we show the average results of the evolution of 100 control orbits and their ranges (minimum and maximum) in the values of the parameters at a given time. The initial orbital elements of each control orbit have been computed varying them randomly, within the ranges defined by their mean values and standard deviations. As pointed out above, this is equivalent to considering a number of different virtual minor planets moving in similar orbits. This approach is reasonable if the orbital solution is the result of stochastic simulations, but it is arguable if that solution is associated with a set of observations obtained for a single minor planet. In this case, the fact that the elements affect each other cannot be neglected and the covariance matrix should be applied.

As a consistency test, we have used an implementation of the classical Monte Carlo using the Covariance Matrix (MCCM; Bordovitsyna et al. 2001; Avdyushev & Banschikova 2007) approach to recompute the past orbital evolution of these objects generating control orbits with initial parameters from the nominal orbit adding random noise on each initial orbital element making use of the covariance matrix (for details, see de la Fuente Marcos & de la Fuente Marcos 2015b). The covariance matrix of the orbit in Table 5 has been computed as described in e.g. Press et al. (2007) using a sample of 19 best solutions in terms of astrometry as described above. The other covariance matrices have been retrieved from the JPL Small-Body Database. Our results are given in Figs. 21–25 and they show that, in general, the difference is not very significant. Figure 21 compares the evolution of the solution in Table 5 (both in terms of standard deviations, black curves, and covariance matrix, grey curves) with the one available from the JPL Small-Body Database (Farnocchia et al. 2016) derived from the covariance matrix available from the JPL Small-Body Database. These solutions are based on different values of the impact parameters, but the short-term evolution of their orbits is fairly similar. Therefore, the detailed discussion made above on the past short-term evolution of 2014 AA as described by our favoured orbital solution applies to the one derived in Farnocchia et al. (2016) as well. For most of the orbits studied here, the average orbital evolution of

samples obtained from the standard deviations matches well the one derived for samples generated using the covariance matrix. The most dramatic difference is found for 2013 NJ_4. Our calculations appear to have uncovered an unexpected stable island in the surveyed volume of the orbital parameter space. Objects moving inside that region are largely unperturbed, with resonances cancelling each other out (see Fig. 26).

8.3 A stable island in a sea of PHAs

The previous section compares the short-term orbital evolution of the objects studied above using initial conditions derived with and without the application of the covariance matrix. Surprisingly, the evolution of meteoroid 2013 NJ_4 as computed using control orbits derived from the covariance matrix exhibits Trojan-like stability. The standard deviations associated with the osculating orbital elements for this object are unusually small for an orbit with an Earth MOID of just 0.0046 AU that is comparable to those of Potentially Hazardous Asteroids (PHAs). The relatively long-term evolution (±500 kyr) of a representative instance of such an orbit is displayed in Fig. 26. The presence of this stable island within their orbital subdomain is another argument in favour of singling out this group of objects among the general NEO population. A dynamically stable island may act as a long-term source of drifting small bodies.

9 Conclusions

The aim of this work was to perform an independent determination of the pre-impact orbit of meteoroid 2014 AA using an improved set of impact parameters for the airburst event. This has been accomplished by applying two different techniques: geometric Monte Carlo and N-body calculations. Our results are consistent with those obtained by other authors using other techniques. The results of a search for minor bodies moving in similar orbits among already known objects and subsequent N-body simulations suggest that 2014 AA might have formed during a relatively recent asteroid break-up. If this somewhat speculative interpretation is correct, 2014 AA would have been a fragment of a parent body and a (probably large) group of meteoroids of similar composition moving in trajectories analogous to that of 2014 AA might exist. Asteroid 2014 AA was comparable in size to 2008 TC_3, the single other example of an impacting object observed prior to atmospheric entry. However, their pre-impact orbital evolutions were rather different. The dynamical evolution of 2014 AA and related objects is also not similar to that of the parent body of the Crete bolide (2002 June 6, Brown et al. 2002) observed over the Mediterranean Sea or the recent Chelyabinsk Event (see e.g. de la Fuente Marcos & de la Fuente Marcos 2013, 2014; de la Fuente Marcos et al. 2015). Our conclusions can be summarized as follows.

- The values of the impact parameters of meteoroid 2014 AA as derived from infrasound data are: ($\lambda_{\rm impact}$, $\phi_{\rm impact}$, $t_{\rm impact}$) = (-43.°7±1.°7, +11.°2±2.°8, 2456659.618±0.011 JD UTC). These values are consistent with the available astrometry.
- In the decades preceding its impact, 2014 AA followed an orbit (a = 1.1623 AU, e = 0.2116, i = 1.°4156, Ω = 101.°6086, and ω = 52.°3393) with perihelion (q = 0.9164 AU) inside the orbit of the Earth and aphelion (Q = 1.4083 AU) beyond Mars' perihelion. These values are equally consistent with the available astrometry.
- Meteoroid 2014 AA was subjected to a Kozai resonance prior to its collision with the Earth and it may have remained in the dynamical neighbourhood of our planet for many thousands of years; however, it may also be a relatively recent fragment spawned from another NEA.
- A search for objects moving in orbits similar to that of 2014 AA gives several tentative candidates. All these objects have remained in the neighbourhood of our planet for thousands of years and some of them, 2014 AA included, could be fragments from a recent break-up.
- Our analysis of the past orbital evolution of 2014 AA and related objects suggests that asteroidal disruption events might not only be taking place in the main belt but also among the closest NEOs. If confirmed, this finding would imply that the asteroid impact hazard associated with bodies small enough to be of less concern could be higher than commonly thought.

Acknowledgements The authors thank the referee, T. J. Jopek, for his constructive, detailed and very helpful reports, S. J. Aarseth for providing one of the codes used in this research and for comments on early versions of this work, S. R. Chesley for providing his results on the pre-impact orbit of 2014 AA prior to publication, D. Farnocchia for his input on early versions of this work, J. D. Giorgini for providing the details of the orbit computed by the JPL, Bill Gray for sharing the early results of his impact calculations, and S. R. Proud for sharing the results of his analysis of some weather satellite imagery. This work was partially supported by the Spanish 'Comunidad de Madrid' under grant CAM S2009/ESP-1496. Some of the calculations discussed in

this paper were completed on the 'Servidor Central de Cálculo' of the Universidad Complutense de Madrid. This research has made use of NASA's Astrophysics Data System, the ASTRO-PH e-print server, the MPC data server, and the NEODyS information service.

References

Aarseth, S.J.: Gravitational N-body simulations, p. 27. Cambridge University Press, Cambridge (2003)

Adamo, D.R.: Horizons Newsletter, June 2011, p. 64 (2011) (http://info.aiaa.org/Regions/SC/Houston/Newsletters/Horizons%202010-12%20Dec%2010.pdf)

Agarwal, J., Jewitt, D., Weaver, H., Mutchler, M., Larson, S.: Astron. J. **151**, 12 (2016)

Avdyushev, V.A., Banschikova, M.A.: Sol. Syst. Res. **41**, 413 (2007)

Baluev, R.V., Kholshevnikov, K.V.: Celest. Mech. Dyn. Astron. **91**, 287 (2005)

Benitez, F., Gallardo, T.: Celest. Mech. Dyn. Astron. **101**, 289 (2008)

Boekholt, T., Portegies Zwart, S.: Comput. Astrophys. Cosmol. **2**, 2 (2015)

Bordovitsyna, T., Avdyushev, V., Chernitsov, A.: Celest. Mech. Dyn. Astron. **80**, 227 (2001)

Borovička, J., Charvát, Z.: Astron. Astrophys. **507**, 1015 (2009)

Bottke, W.F., Jr., Vokrouhlický, D., Rubincam, D.P., Nesvorný, D.: Annu. Rev. Earth Planet. Sci. **34**, 157 (2006)

Box, G.E.P., Muller, M.E.: Ann. Math. Stat. **29**, 610 (1958)

Brachet, N., Brown, D., Le Bras, R., Mialle, P., Coyne, J.: In: Le Pichon, A., Blanc, E., Hauchecorne, A., (eds.) Infrasound Monitoring for Atmospheric Studies, p. 77. Springer, Berlin (2010)

Brown, P.: In: Muinonen, K., Penttilä, A., Granvik, M., Virkki, A., Fedorets, G., Wilkman, O., Kohout, T., (eds.) Asteroids, Comets, Meteors – Book of Abstracts, p. 84. Helsinki, Finland (2014)

Brown, P., Spalding, R.E., ReVelle, D.O., Tagliaferri, E., Worden, S.P.: Nature **420**, 294 (2002)

Brown, P.G., et al.: Nature **503**, 238 (2013)

Brož, M., Vokrouhlický, D.: Mon. Not. R. Astron. Soc. **390**, 715 (2008)

Čapek, D., Vokrouhlický, D.: Astron. Astrophys. **519**, A75 (2010)

Ceplecha, Z.: Bull. Astron. Inst. Czechoslov. **38**, 222 (1987)

Chesley, S.R., Milani, A.: Bull. Am. Astron. Soc. **31**, 1117 (1999)

Chesley, S.R., Farnocchia, D., Brown, P., Chodas, P.W.: AAS/Division for Planetary Sciences Meeting Abstracts **46**, 403.03 (2014)

Chesley, S.R., Farnocchia, D., Brown, P., Chodas, P.W.: Proceedings of the Aerospace Conference, 2015 IEEE. 7–14 March 2015. Big Sky, MT (2015) (doi: 10.1109/AERO.2015.7119148)

Chodas, P.W., Yeomans, D.K.: In: Noll, K.S., Weaver, H.A., Feldman, P.D., (eds.) IAU Colloq. 156: The Collision of Comet Shoemaker-Levy 9 and Jupiter, p. 1. Cambridge University Press, Cambridge (1996)

Chodas, P., Chesley, S., Yeomans, D.: AAS/Division for Planetary Sciences Meeting Abstracts **41**, 9.05 (2009)

de la Fuente Marcos, C., de la Fuente Marcos, R.: Mon. Not. R. Astron. Soc. **427**, 728 (2012)

de la Fuente Marcos, C., de la Fuente Marcos, R.: Mon. Not. R. Astron. Soc. **436**, L15 (2013)

de la Fuente Marcos, C., de la Fuente Marcos, R.: Mon. Not. R. Astron. Soc. **443**, L39 (2014)

de la Fuente Marcos, C., de la Fuente Marcos, R.: Mon. Not. R. Astron. Soc. **446**, L31 (2015a)

de la Fuente Marcos, C., de la Fuente Marcos, R.: Mon. Not. R. Astron. Soc. **453**, 1288 (2015b)

de la Fuente Marcos, C., de la Fuente Marcos, R., Aarseth, S.J.: Astrophys. Space Sci. **357**, 60 (2015c)

de la Fuente Marcos, C., de la Fuente Marcos, R.: Mon. Not. R. Astron. Soc. **456**, 2946 (2016)

Denneau, L., et al.: Icarus **245**, 1 (2015)

Dmitriev, V., Lupovka, V., Gritsevich, M.: Planet. Space Sci. **117**, 223 (2015)

Dorschner, J.: Astron. Nachr. **295**, 141 (1974)

Drahus, M., Waniak, W., Tendulkar, S., Agarwal, J., Jewitt, D., Sheppard, S.S.: Astrophys. J. **802**, L8 (2015)

Drummond, J.D.: Icarus **45**, 545 (1981)

Eastman, J., Siverd, R., Gaudi B.S.: Publ. Astron. Soc. Pac. **122**, 935 (2010)

Farnocchia, D., Chesley, S.R., Vokrouhlický, D., Milani, A., Spoto, F., Bottke, W.F.: Icarus **224**, 1 (2013)

Farnocchia, D., Chesley, S.R., Micheli, M.: Icarus **258**, 18 (2015)

Farnocchia, D., Chesley, S.R., Brown, P.G., Chodas, P.W.: Icarus **274**, 327 (2016)

Foglia, S., Masi, G.: Minor Planet Bull. **31**, 100 (2004)

Giorgini, J.D., et al.: Bull. Am. Astron. Soc. **28**, 1158 (1996)

Giorgini, J.D., Yeomans, D.K.: On-Line System Provides Accurate Ephemeris and Related Data, NASA TECH BRIEFS, NPO-20416, p. 48 (1999)

Giorgini, J.D., Chodas, P.W., Yeomans, D.K.: Orbit Uncertainty and Close-Approach Analysis Capabilities of the Horizons On-Line Ephemeris System, 33rd AAS/DPS meeting, New Orleans, LA (2001)

Green, D.N., Bowers, D.: J. Geophys. Res. **115**, D18116 (2010)

Greenstreet, S., Ngo, H., Gladman, B.: Icarus **217**, 355 (2012)

Gronchi, G.: Celest. Mech. Dyn. Astron. **93**, 295 (2005)

Hirayama, K.: Astron. J. **31**, 185 (1918)

Ito, T., Tanikawa, K.: Icarus **139**, 336 (1999)

Ito, T., Tanikawa, K.: Mon. Not. R. Astron. Soc. **336**, 483 (2002)

Jenniskens, P.: Meteor Showers and Their Parent Comets. Cambridge University Press, Cambridge (2006)

Jenniskens, P.: In: Muinonen, K., Penttilä, A., Granvik, M., Virkki, A., Fedorets, G., Wilkman, O., Kohout, T., (eds.) Asteroids, Comets, Meteors – Book of Abstracts, p. 263. Helsinki, Finland (2014)

Jenniskens, P., et al.: Nature **458**, 485 (2009)

Jewitt, D.: Astron. J. **143**, 66 (2012)

Jewitt, D., Hsieh, H., Agarwal, J.: In: Michel, P., DeMeo, F.E., Bottke, W.F. Jr., (eds.) Asteroids IV, p. 221. University of Arizona Space Science Series, University of Arizona Press, Tucson (2015)

Jopek, T.J., Williams, I.P.: Mon. Not. R. Astron. Soc. **430**, 2377 (2013)
Jopek, T.J., Kanuchová, Z.: In: Jopek, T.J., Rietmeijer, F.J.M., Watanabe, J., Williams, I.P., (eds.) The Meteoroids 2013, p. 353. Adam Mickiewicz University Press, Poznan, Poland (2014)
Kowalski, R.A., et al.: MPEC 2011-J37 (2011)
Kowalski, R.A., et al.: MPEC 2014-A02 (2014)
Kozai, Y.: Astron. J. **67**, 591 (1962)
Kozubal, M.J., Gasdia, F.W., Dantowitz, R.F., Scheirich, P., Harris, A.W.: Meteorit. Planet. Sci. **46**, 534 (2011)
Le Pichon, A., Ceranna, L., Vergoz, J.: J. Geophys. Res. **117**, D05121 (2012)
Le Pichon, A., et al.: Geophys. Res. Lett. **40**, 3732 (2013)
Lindblad, B.A.: In: Kozai, Y., Binzel, R.P., Hirayama, T., (eds.) Seventy-five Years of Hirayama Asteroid Families: the Role of Collisions in the Solar System History. ASP Conference Series, vol. 63, p. 62 (1994)
Lindblad, B.A., Southworth, R.B.: In: Gehrels, T., (ed.) Physical Studies of Minor Planets. NASA SP-267, p. 337. NASA, Washington (1971)
Makino, J.: Astrophys. J. **369**, 200 (1991)
Maxwell, A.D.: Astron. J. **42**, 13 (1932)
McMillan, R.S., et al.: MPEC 2011-G32 (2011)
Metropolis, N., Ulam, S.: J. Am. Stat. Assoc. **44**, 335 (1949)
Michel, P.: Astron. Astrophys. **328**, L5 (1997)
Michel, P., Thomas, F.: Astron. Astrophys. **307**, 310 (1996)
Micheli, M., Tholen, D.J., Lister, T., Primak, N., Schultz, A., Watters, S., Thiel, J., Goggia, T.: MPEC 2012-D104 (2012)
Milani, A., Carpino, M., Hahn, G., Nobili, A.M.: Icarus **78**, 212 (1989)
Milani, A., Knežević, Z.: Celest. Mech. Dyn. Astron. **92**, 1 (2005)
Montenbruck, O., Pfleger, T.: Astronomy on the Personal Computer, 4th edn. Springer, Heidelberg (2000)
Murray, C.D., Dermott, S.F.: Solar System Dynamics, p. 97. Cambridge University Press, Cambridge (1999)
Namouni, F.: Icarus **137**, 293 (1999)
Olech, A., et al.: Mon. Not. R. Astron. Soc. **454**, 2965 (2015)
Oszkiewicz, D., Muinonen, K., Virtanen, J., Granvik, M., Bowell, E.: Planet. Space Sci. **73**, 30 (2012)
Pilger, C., Ceranna, L., Ross, J.O., Le Pichon, A., Mialle, P., Garcés, M.A.: Geophys. Res. Lett. **42**, 2523 (2015)
Popova, O.P., et al.: Science **342**, 1069 (2013)
Porubcan, V., Kornoš, L., Williams, I.P.: Contributions of the Astronomical Observatory Skalnaté, vol. 36, no. 2, p. 103 (2006)
Press, W.H., Teukolsky, S.A., Vetterling, W.T., Flannery, B.P.: Numerical Recipes: The Art of Scientific Computing, 3rd edn. Cambridge University Press, Cambridge (2007)
Richardson, D.C., Bottke, W.F., Love, S.G.: Icarus **134**, 47 (1998)
Ries, J.G., et al.: MPEC 2013-H34 (2013)
Ryan, E.V.: Annu. Rev. Earth Planet. Sci. **28**, 367 (2000)
Sariya, D.P., Yadav, R.K.S.: Astron. Astrophys. **584**, A59 (2015)
Scholz, R.-D., et al.: Astron. Astrophys. **137**, 305 (1999)
Schunová, E., Granvik, M., Jedicke, R., Gronchi, G., Wainscoat, R., Abe, S.: Icarus **220**, 1050 (2012)
Schunová, E., Jedicke, R., Walsh, K.J., Granvik, M., Wainscoat, R.J., Haghighipour, N.: Icarus **238**, 156 (2014)
Šegan, S., Milisavljević, S., Marčeta, D.: Acta Astron. **61**, 275 (2011)
Sitarski, G.: Acta Astron. **48**, 547 (1998)
Sitarski, G.: Acta Astron. **49**, 421 (1999)
Sitarski, G.: Acta Astron. **56**, 283 (2006)
Smart, W.M.: Textbook on Spherical Astronomy, 6th edn., p. 204. Cambridge University Press, Cambridge (1977)
Southworth, R.B., Hawkins, G.S.: Smithson. Contrib. Astrophys. **7**, 261 (1963)
Standish, E.M.: JPL Planetary and Lunar Ephemerides, DE405/LE405. Interoffice Memo. 312.F-98-048, NASA JPL (1998)
Tanikawa, K., Ito, T.: Publ. Astron. Soc. Jpn. **59**, 989 (2007)
Tóth, J., Vereš, P., Kornoš, L.: Mon. Not. R. Astron. Soc. **415**, 1527 (2011)
Trigo-Rodríguez, J.M., et al.: Mon. Not. R. Astron. Soc. **382**, 1933 (2007)
Unnikrishnan, R., Lalonde, J.-F., Vandapel, N., Hebert, M.: Int. J. Comput. Geom. Appl. **20**, 543 (2010)
Valsecchi, G.B., Jopek, T.J., Froeschlé, C.: Mon. Not. R. Astron. Soc. **304**, 743 (1999)
Vokrouhlický, D., Farnocchia, D., Čapek, D., Chesley, S.R., Pravec, P., Scheirich, P., Müller, T.G.: Icarus **252**, 277 (2015)
Wainscoat, R.J., et al.: MPEC 2013-N13 (2013)
Wall, J.V., Jenkins, C.R.: Practical Statistics for Astronomers, 2nd edn. Cambridge University Press, Cambridge (2012)
Walsh, K.J., Richardson, D.C., Michel, P.: Nature **454**, 188 (2008)
Wiśniowski, T., Rickman, H.: Acta Astron. **63**, 293 (2013)
Zappalà, V., Cellino, A., Farinella, P., Knežević, Z.: Astron. J. **100**, 2030 (1990)
Zappalà, V., Cellino, A., Farinella, P., Milani, A.: Astron. J. **107**, 772 (1994)

This 2-column preprint was prepared with the AAS LaTeX macros v5.2.

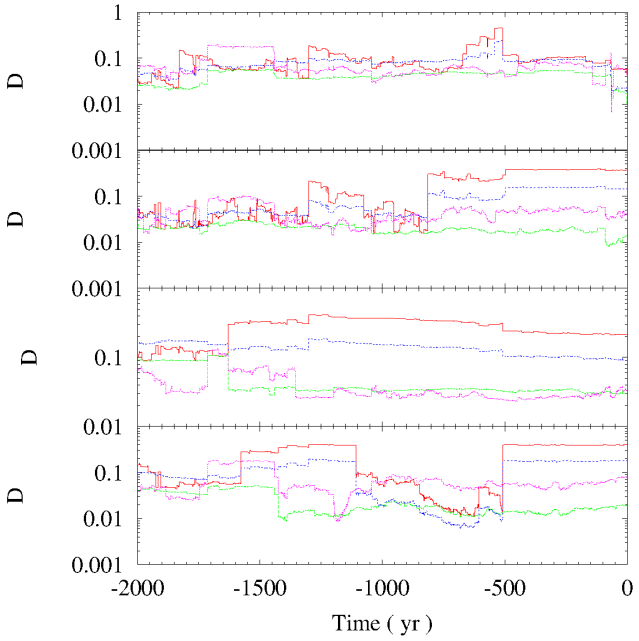

Fig. 19 Average time evolution of the various D-criteria —$D_{\rm SH}$ (red), $D_{\rm LS}$ (green), $D_{\rm D}$ (blue), and $D_{\rm R}$ (pink)— for 2011 JV_{10} (top panel), 2011 GJ_3 (second to top panel), 2012 DJ_{54} (third to top panel), and 2013 NJ_4 (bottom panel) with respect to 2014 AA as described by the solution displayed in Table 5. The values have been computed using the data in Figure 18, left-hand panels.

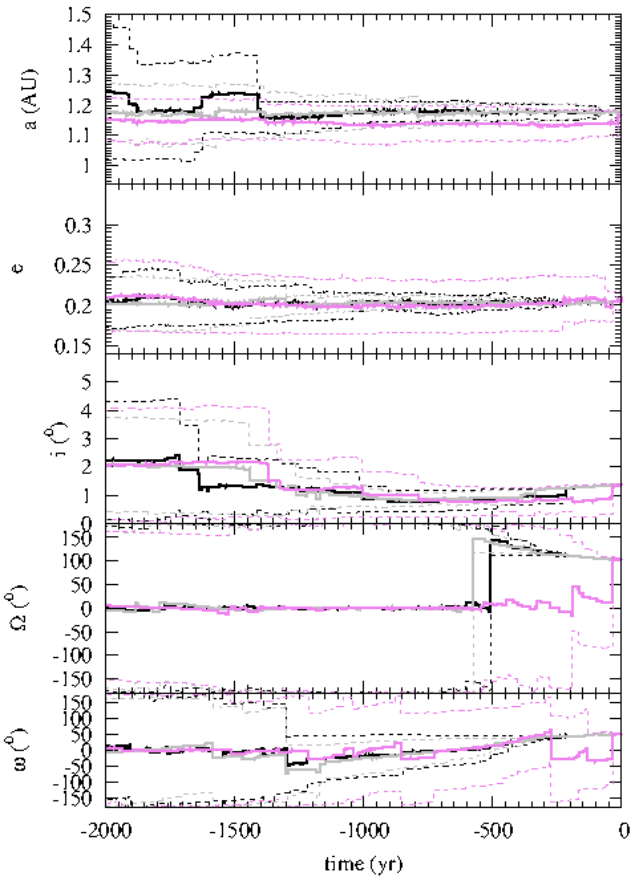

Fig. 21 Time evolution of the orbital elements a, e, i, Ω, and ω of 2014 AA. In black, we plot data derived from the orbit in Table 5 (same data as in Fig. 18), in grey we show the results based on MCCM for the same orbital solution (see the text for details), and in violet we display the results based on MCCM for the orbit available from the JPL Small-Body Database (see the text for details, Farnocchia et al. 2016). In this figure both average values and their ranges are plotted.

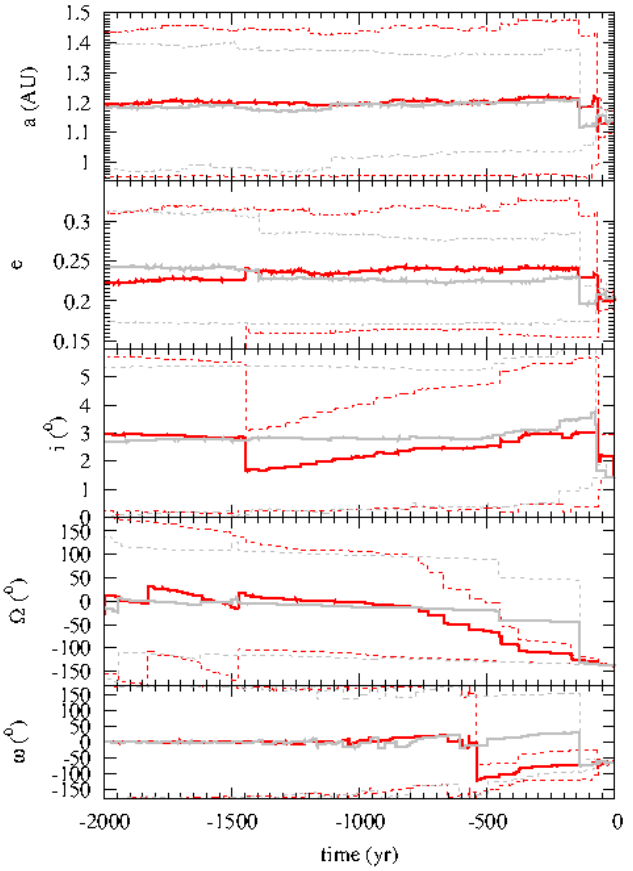

Fig. 22 Time evolution of the orbital elements a, e, i, Ω, and ω of 2011 JV_{10}. In red, we replot the data in Fig. 18, in grey we show the results based on MCCM (see the text for details). In this figure both average values and their ranges are plotted.

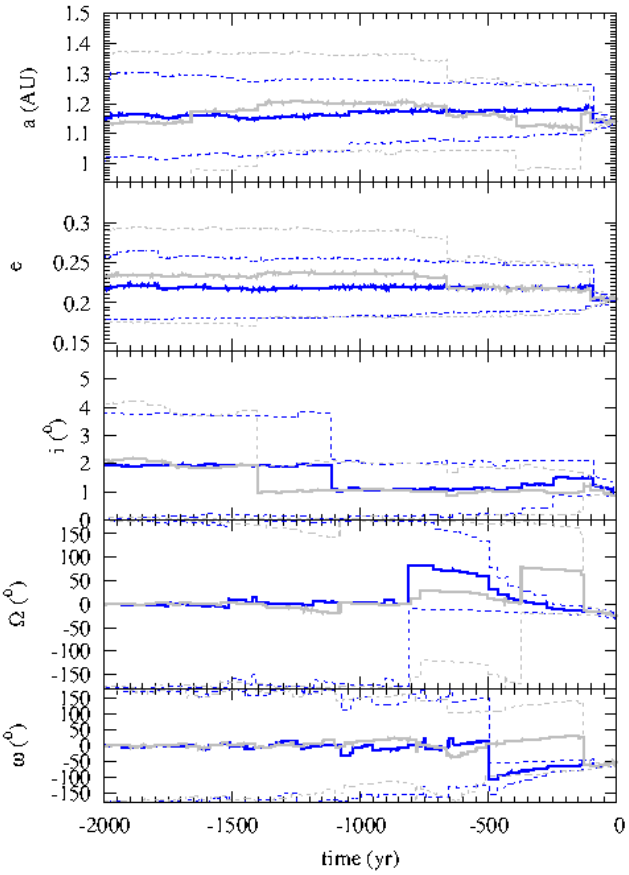

Fig. 23 Same as Fig. 22 but for 2011 GJ_3.

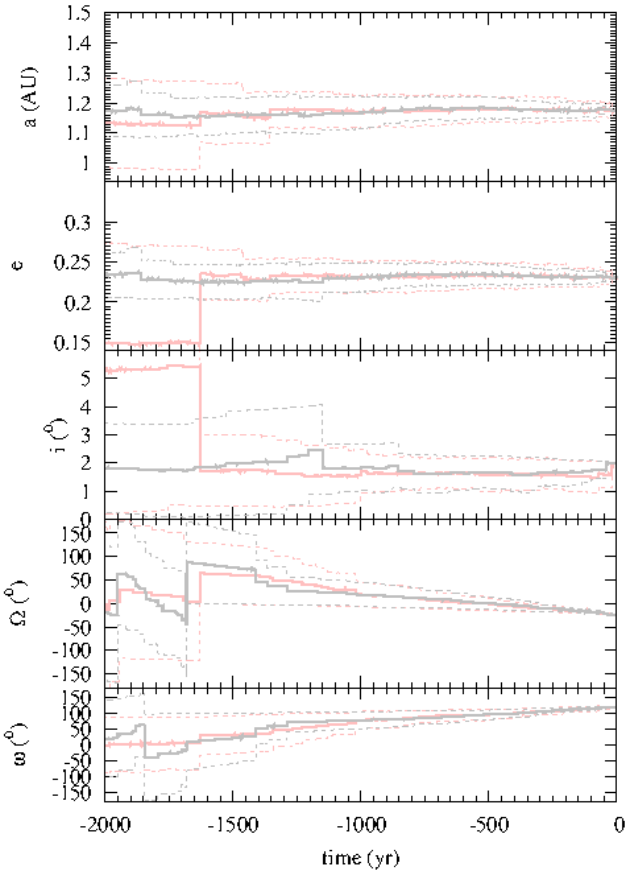

Fig. 24 Same as Fig. 22 but for 2012 DJ_{54}.

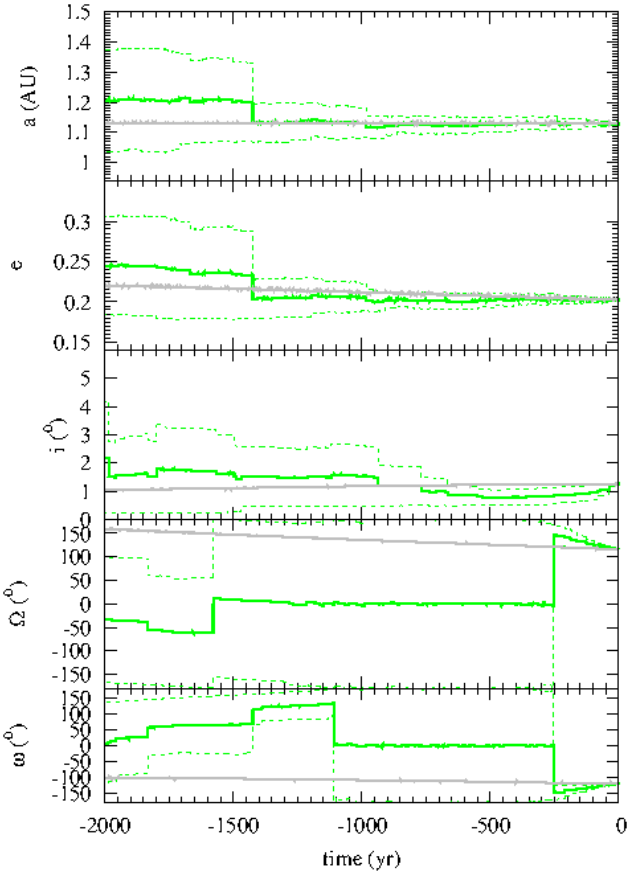

Fig. 25 Same as Fig. 22 but for 2013 NJ_4.

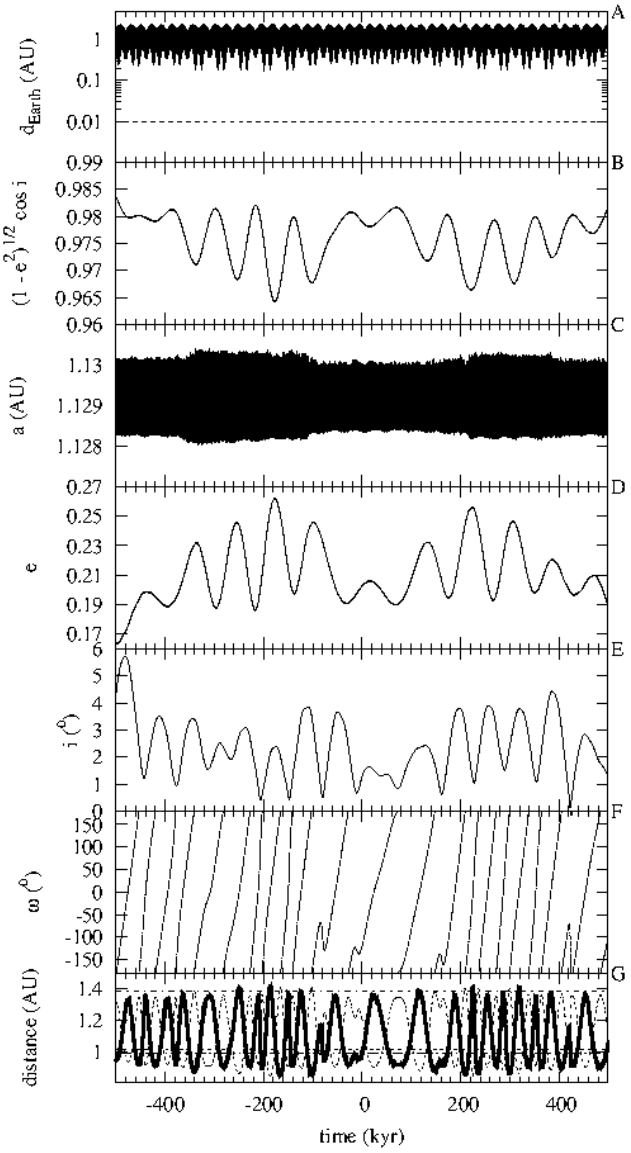

Fig. 26 Same as Fig. 16 but for a representative orbit belonging to the stable island described in the text.

A Orbital elements of the Earth around the time of impact

Chesley et al. (2015) have released the impact time and the hypocentre location for the 2014 AA impact (see their table 1) as included in the REB of the IDC of the CTBTO for 2014 January 2. The impact time was 2014 January 2 at 3:05:25 UTC with an uncertainty of 632 s. The impact location coordinates were latitude (°N) equal to $+14\overset{\circ}{.}6326$ and longitude (°E) of $-43\overset{\circ}{.}4194$. Therefore, the actual impact with the atmosphere took place at epoch 2456659.629537 Julian Date, Barycentric Dynamical Time. The uncertainty is about 10 minutes. The osculating orbital elements of the Earth within ±150 s of the detection are given in Table 10. These values have been computed by the SSDG, HORIZONS On-Line Ephemeris System.

Table 10 Orbital elements of the Earth around JD 2456659.629537 = A.D. 2014-Jan-02 03:06:32.00 TDB (Source: JPL Horizons system). Data as of 2016 April 12.

Epoch JD TDB	TDB	a (AU)	e	i (°)	Ω (°)	ω (°)	f (°)
2456659.627777778	03:04:00.0	1.000972380029170	0.01761703261345213	0.001880262202725939	196.1937930138271	266.8968539832863	358.3453037378698
2456659.628472222	03:05:00.0	1.000972354161487	0.01761700936572361	0.001880231304943617	196.1824664060930	266.9084313181994	358.3457610767323
2456659.629166667	03:06:00.0	1.000972328266890	0.01761698609092967	0.001880200483856643	196.1711389039578	266.9200095419956	358.3462184211128
2456659.629537037	03:06:32.0	1.000972314445433	0.01761697366663995	0.001880184077304693	196.1650972042493	266.9261849576632	358.3464623403758
2456659.629861111	03:07:00.0	1.000972302345379	0.01761696278907163	0.001880169739474883	196.1598105087923	266.9315886532928	358.3466757710223
2456659.630555556	03:08:00.0	1.000972276396955	0.01761693946014976	0.001880139071808320	196.1484812220189	266.9431686506603	358.3471331264694
2456659.631250000	03:09:00.0	1.000972250421621	0.01761691610416575	0.001880108480869461	196.1371510449252	266.9547495327997	358.3475904874647

B Cartesian state vectors at epoch JD TDB 2456658.628472222 = A.D. 2014-Jan-1 03:05:00.0000 TDB

In order to facilitate verification of our results by other astrodynamicists, we show in Table 11 the Cartesian state vectors of the physical model used in all the calculations presented here. These values have been computed by the SSDG, HORIZONS On-Line Ephemeris System at epoch JD TDB 2456658.628472222 = A.D. 2014-Jan-01 03:05:00.0000 TDB, this instant is considered as $t = 0$ across this work unless explicitly stated. Positions and velocities are referred to the barycentre of the Solar System.

Table 11 Cartesian state vectors at epoch JD TDB 2456658.628472222 that corresponds to 03:05:00.0000 TDB on 2014 January 1 (Source: JPL Horizons system, data as of 2016 April 12). The sample Cartesian vector for 2014 AA corresponds to the nominal orbit in Table 5.

Body	Mass (kg)	X (AU)	Y (AU)	Z (AU)	$V_{\rm X}$ (AU/day)	$V_{\rm Y}$ (AU/day)	$V_{\rm Z}$ (AU/day)
Sun	1.988544E+30	9.876557315045510E-04	-2.277483052076684E-03	-9.309130493714816E-05	6.061452466600682E-06	2.330421391102359E-06	-1.404175947545831E-07
Mercury	3.302E+23	1.234712512947228E-01	-4.353820916108924E-01	-4.671846192551433E-02	2.143843797991616E-02	9.091989724464501E-03	-1.223863011823374E-03
Venus	48.685E+23	-5.149511742679028E-02	7.151279710261775E-01	1.276613490638690E-02	-2.023520017529031E-02	-1.582388301347185E-03	1.146311987350358E-03
Earth	5.97219E+24	-1.768146919670241E-01	9.648703577630898E-01	-1.251184107370999E-04	-1.720245307304753E-02	-3.173746202131230E-03	-3.541894002146146E-07
Moon	734.9E+20	-1.765843263680927E-01	9.624988926026269E-01	5.765116799479567E-05	-1.657120668505812E-02	-3.100270805332192E-03	2.659631061553224E-05
Mars	6.4185E+23	-1.512135183594610E+00	6.930582722833578E-01	5.161676323389820E-02	-5.312436625323014E-03	-1.151792918278832E-02	-1.109714131381030E-04
(1) Ceres	9.393E+20	-2.532553587303031E+00	2.006361724318938E-02	4.677363530307643E-01	-4.977519833731861E-04	-1.106269591780204E-02	-2.549781096676565E-04
(2) Pallas	2.108E+20	-1.446164856316815E+00	1.343011887296409E+00	-8.086050115131924E-01	-9.795008211501307E-03	-6.689790295651018E-03	5.443421539610216E-03
(4) Vesta	2.59076E+20	-2.280182334607567E+00	2.789898573544310E-01	2.689336672805309E-01	-3.557060360882084E-04	-1.140592407389319E-02	3.860042747257529E-04
Jupiter	1898.13E+24	-1.330758770698398E+00	5.016245845201770E+00	8.864460103589159E-03	-7.385422526176123E-03	-1.576169860785649E-03	1.718627296846660E-04
Saturn	5.68319E+26	-6.883730900143171E+00	-7.078257667923089E+00	3.970324150311733E-01	3.695935133299771E-03	-3.904438907150792E-03	-7.891989877674008E-05
Uranus	86.8103E+24	1.964589537999795E+01	3.920793902887398E+00	-2.399582673853207E-01	-7.984941344501358E-04	3.673711191904133E-03	2.400439209208154E-05
Neptune	102.41E+24	2.706460640088594E+01	-1.289376969420147E+01	-3.582088655530658E-01	1.328799214346798E-03	2.852447990866922E-03	-8.914679327416514E-05
Pluto-Charon barycentre	1.45712E+22	6.258166791449586E+00	-3.192714938519402E+01	1.606170877827874E+00	3.141405466621021E-03	-2.968297792659612E-05	-9.055043888369047E-04
Nominal impactor	4.0E+04	-1.7644464556E-01	9.6798951463E-01	-6.2289614E-04	-1.756498228E-02	-6.03688848E-03	4.5521881E-04